Twelve modified figures of merit of 2–2-type composites based on relaxor-ferroelectric single crystals

A. N. Isaeva[a], V. Yu. Topolov,[a,*] C. R. Bowen,[b] and J. I. Roscow[b]

[a] *Department of Physics, Southern Federal University, 5 Zorge Street, 344090 Rostov-on-Don, Russia*

[b] *Department of Mechanical Engineering, University of Bath, Bath, BA2 7AY, United Kingdom*

ABSTRACT Twelve modified figures of merit are studied for the first time for 2–2-type composites based on relaxor-ferroelectric single crystals such as [001]-poled $(1 - x)Pb(A_{1/3}Nb_{2/3})O_3 - xPbTiO_3$, where A = Mg or Zn. These modified figures of merit are related to the piezoelectric coefficients d_{3j}^* of the composite (j = 1, 2 and 3) and characterise the effectiveness of energy harvesting and transduction along the three co-ordinate axes OX_j of a piezoelectric composite under a constant mechanical stress or strain. The volume-fraction dependencies of the modified figures of merit are analysed for parallel-connected 2–2 and 2–2–0 composites, and the effect of porosity (i.e. the volume fraction and shape of air pores in each polymer layer) on these figures of merit is considered for 2–2–0 composites. Linkages between the modified figures of merit and traditional energy-harvesting figures of merit $d_{3j}^* g_{3j}^*$ are discussed for the studied 2–2-type composites. New diagrams are developed to indicate important volume-fraction ranges that correspond to a large anisotropy of exemplar modified figures of merit. Due to the large effective parameters and large anisotropy of specific figures of merit, the studied composites are of interest in piezoelectric sensor, transducer and energy-harvesting applications.

Keywords: Piezo-active composite; Figure of merit; Relaxor-ferroelectric single crystal; Porous polyurethane

---

* Corresponding author. *E-mail address:* vutopolov@sfedu.ru (V.Yu. Topolov).

1. Introduction

Piezo-active composites based on relaxor-ferroelectric single crystals (SCs) [1, 2] with outstanding electromechanical properties [3, 4] are regarded as promising modern piezoelectric energy-harvesting materials [5, 6]. Among the relaxor-ferroelectric SC components, the domain-engineered $(1 - x)Pb(Mg_{1/3}Nb_{2/3})O_3 - xPbTiO_3$ (PMN–*x*PT) and $(1 - y)Pb(Zn_{1/3}Nb_{2/3})O_3 - yPbTiO_3$ (PZN–*y*PT) SCs, and their compositions near the morphotropic phase boundary, are of particular interest [5, 6]. Composites based on these SCs poled in specific crystallographic directions [3, 4, 6] are attractive for their high performance in a variety of piezotechnical, hydroacoustic, and energy harvesting transducer applications [4–6]. The effectiveness of the application of piezo-active composites for transducers and energy-harvesting systems depends [6, 7] on electromechanical coupling factors (ECFs)

$$k_{ij}^{*} = d_{ij}^{*}(\varepsilon_{ii}^{*\sigma} s_{jj}^{*E})^{-1/2} \quad (1)$$

and traditional (or squared) figures of merit (FOMs)

$$(Q_{ij}^{*})^2 = d_{ij}^{*} g_{ij}^{*} \quad (2)$$

where d_{ij}^{*} is the piezoelectric charge coefficient, g_{ij}^{*} is the piezoelectric voltage coefficient, $\varepsilon_{ii}^{*\sigma}$ is the absolute dielectric permittivity and s_{jj}^{*E} is the elastic compliance; the asterisk (*) notation signifies the *effective* properties of the piezo-active composite material. In specific applications, mechanical and electric quality factors, piezoelectric anisotropy, sensitivity [6, 8], and other characteristics of piezo-active composites can also be taken into account.

In 2019, a new series of *modified FOMs* was proposed to estimate the effectiveness of a piezoelectric sample under mechanical stress σ or strain ξ [9], where the modified FOMs associated with the longitudinal and transverse piezoelectric effects were studied numerically for poled porous ferroelectric ceramics. In the same year, porous ferroelectric PZT-type ceramics were used as components of novel laminar composites with 2–0–2 [10] and 2–0–2–0 [11] connectivity patterns, and large values of the FOM $(Q_{33}^{*})^2$ from Eq. (2) were first achieved and analysed for a 2–0–2–0 composite with two systems of pores. Furthermore, an excellent electric output of the 2–2 composite based on relaxor-ferroelectric SC [12] showed promise for high-performance devices in the area of biomechanical motion sensors and piezoelectric energy harvesting. A novel flexible wireless energy harvester and sensor [13] based on a composite, containing a porous electret piezoelectric PVDF-based polymer, exhibited improved piezoelectric and dielectric properties in comparison to the polymer component. The high power density, effective energy conversion and sensitivity of the harvester [13] demonstrated the potential for these materials to play an important role in a range of transducer applications. A successful combination of a $(Pb, La)(Zr, Ti)O_3$ ferroelectric ceramic, polyvinylidene fluoride

polymer and multi-walled carbon nanotubes enabled Pal et al. [14] to achieve improved piezoelectric and energy-storage characteristics in a novel three-component composite, in comparison to the similar two-component ceramic / polymer composites. However, to date, the modified FOMs known from work [9] have yet to be studied for 2–2-type composites based on the aforementioned relaxor-ferroelectric SCs. The aim of the present paper is to study the modified FOMs for the system that are related to the longitudinal and transverse piezoelectric effects in the 2–2 and 2–2–0 composites based on either PMN–*x*PT or PZN–*y*PT SCs. It should be added that the piezo-active 2–2-type composites can be manufactured by a variety of methods [10–12, 14] that are suitable for fabricating novel composites based on relaxor-ferroelectric SCs poled along specific crystallographic directions.

2. Model concepts, methods and components

2.1. Model of the piezo-active 2–2-type composite

In the present paper we study the performance of the parallel-connected 2–2-type composites with a regular distribution of the SC and polymer layers in the OX_1 direction, as shown in Fig. 1. The layers of each composite have their long dimension in the OX_2 and OX_3 directions. The first layer type is considered to be a domain-engineered SC, see inset 1 in Fig. 1, and this SC is poled along OX_3. The main crystallographic axes of the domain-engineered SC are oriented as follows: $X \parallel [001] \parallel OX_1$, $Y \parallel [010] \parallel OX_2$ and $Z \parallel [001] \parallel OX_3$.

The second layer type is either monolithic polymer (inset 2 in Fig. 1) or porous polymer with 3–0 connectivity (inset 3 in Fig. 1). In the porous polymer layer, the air pores are described by the equation

$$(x_1 / a_{1,p})^2 + (x_2 / a_{2,p})^2 + (x_3 / a_{3,p})^2 = 1, \quad (3)$$

where $a_{1,p}$, $a_{2,p} = a_{1,p}$ and $a_{3,p}$ are semi-axes of the spheroid from Eq. (3). Hereafter we use the aspect ratio $\rho_p = a_{1,p} / a_{3,p}$ and volume fraction m_p to characterise the spheroidal shape and volume fraction of the air pores, respectively. Both ρ_p and m_p are related to the second layer type shown in inset 3 of Fig. 1. The air pores are distributed regularly in the polymer medium, and their centres of symmetry form a simple parallelepiped lattice. The SC / monolithic polymer composite is characterised by 2–2 connectivity in terms of work [6, 15], and the SC / porous polymer composite is described by 2–2–0 connectivity. In both these composites, the poling direction is the OX_3 axis shown in Fig. 1.

2.2. Methods to find effective properties and related parameters of composites

The effective elastic, piezoelectric and dielectric (i.e., electromechanical) properties of the 2–2 composite were determined by means of the matrix method [6, 16] that takes into account

the electromechanical interaction between the layers. A matrix of the effective properties of the 2–2 composite is given by

$$|| C^{*} || = [|| C^{(1)} ||\cdot|| M || m + || C^{(2)} || (1 - m)] [|| M || m + || I || (1 - m)]^{-1}, \quad (4)$$

where

$$|| C^{(n)}|| = \begin{pmatrix} || s^{(n),E} || & || d^{(n)} ||^{t} \\ || d^{(n)} || & || \varepsilon^{(n),\sigma} || \end{pmatrix} \quad (5)$$

is the 9 × 9 matrix that characterises the properties of the SC (n = 1) or polymer (n = 2) component. In Eq. (4), m is the volume fraction of the SC layers. || M || is the 9 × 9 matrix related to the boundary conditions at interfaces x_1 = constant (see Fig. 1), and || I || is the 9 × 9 identity matrix. The || $C^{(n)}$ || matrix from Eq. (5) contains a 6 × 6 matrix of elastic compliances || $s^{(n),E}$ || at electric field E = constant, the 6 × 3 matrix of piezoelectric coefficients || $d^{(n)}$ ||, the 3 × 3 matrix of dielectric permittivities || $\varepsilon^{(n),\sigma}$ || at σ = constant, and the superscript t is introduced to show the matrix transposition. The matrices of properties || $C^{(1)}$ || and || $C^{(2)}$ || from Eq. (4) belong to the components that can be from any symmetry class. The effective electromechanical properties of the 2–2 composite were determined in a long-wave approximation [6], whereby any wavelength from an external field is much longer than the thickness of separate layers of the composite sample, as shown in Fig. 1.

The effective electromechanical properties of the 2–2–0 composite were found in two stages. In the first stage, the effective properties of the porous polymer matrix (see inset 3 in Fig. 1) were determined as a function of the aspect ratio ρ_p of the pores and their volume fraction (porosity) m_p in the polymer layer type. This determination is based on Eshelby's concept of spheroidal inclusions in heterogeneous solids [17, 18]. The effective properties of the porous polymer medium with 3–0 connectivity are represented in the matrix form [18] as follows:

$$|| K^{(3\text{-}0)} || = || K^{(2)} || [|| I || - m_p(|| I || - (1 - m_p)|| S ||)^{-1}] . \quad (6)$$

In Eq. (6), || $K^{(2)}$ || is the 9 × 9 matrix of the properties of the polymer component, || I || is the identity matrix, and || S || is the matrix that comprises components of the electroelastic Eshelby tensor. The || S || elements depend on the aspect ratio ρ_p of the pore and on the properties of polymer [17]. The properties of the polymer component are given by

$$|| K^{(2)} || = \begin{pmatrix} || c^{(2),E} || & || e^{(2)} ||^{t} \\ || e^{(2)} || & -|| \varepsilon^{(2),\xi} || \end{pmatrix}. \quad (7)$$

In Eq. (7), || $c^{(2),E}$ || is the 6 × 6 matrix of elastic moduli measured at E = constant, || $e^{(2)}$ || is the 3 × 6 matrix of piezoelectric coefficients, and || $\varepsilon^{(2),\xi}$ || is the 3 × 3 matrix of dielectric permittivities at ξ = constant. The structure of the || $K^{(3\text{-}0)}$ || matrix from Eq. (6) is similar to the || $K^{(2)}$ ||

structure, and the $\| K^{(3\text{-}0)} \|$ elements are found in the long-wave approximation [6]. This approximation indicates that the longest semi-axis of each air pore is much smaller than the thickness of any layer of the 2–2–0 composite. The $\| K^{(3\text{-}0)} \|$ matrix was used to form the $\| C^{(2)} \|$ matrix involved in Eq. (4), and a transition from the $\| K^{(3\text{-}0)} \|$ elements to the $\| C^{(2)} \|$ elements was performed in terms of formulae [19] for a piezoelectric medium.

During the second stage, we determined the effective properties of the 2–2–0 composite in accordance with Eq. (4). In this case, the $\| C^* \|$ matrix from Eq. (4) depends on m, m_p and ρ_p. Based on the $\| C^* \|$ elements from Eq. (4), we determined the set of effective parameters of the composite, including its ECFs k_{ij}^* from Eq. (1), FOMs $(Q_{ij}^*)^2$ from Eq. (2), and the full set of modified FOMs. In the present study, we present results based on the modified FOMs concerned with the longitudinal (ij = 33) or lateral (ij = 31 and 32) piezoelectric effect in the 2–2-type composites.

The modified FOMs, introduced to characterise an effectiveness of a piezoelectric material in terms of its ability to convert input mechanical to useable electrical energy [9, 20]; this includes

(i) the transmission coefficient that represents the maximum ‘output electrical energy / input mechanical energy’ ratio

$$\lambda_{3j,m}^* = [(k_{3j}^*)^{-1} - ((k_{3j}^*)^{-2} - 1)^{1/2}]^2, \quad (8)$$

(ii) the ‘maximum output electrical energy / stored electrical energy’ ratio

$$L_{3j}^* = \lambda_{3j,m}^* / (k_{3j}^*)^2, \quad (9)$$

(iii) the FOM for a stress-driven harvester

$$F_{3j}^{*\sigma} = L_{3j}^* (Q_{3j}^*)^2, \quad (10)$$

and

(iv) the FOM for a strain-driven harvester

$$F_{3j}^{*\xi} = F_{3j}^{*\sigma} / (s_{jj}^{*E} s_{jj}^{*D}), \quad (11)$$

where j = 1, 2 and 3. In Eqs. (9) and (10), k_{3j}^* are ECFs from Eq. (1). In Eq. (10), $(Q_{3j}^*)^2$ are traditional FOMs [see Eq. (2)] that are important to estimate the ‘signal / noise’ ratio of a piezoelectric device [6]. In Eq. (11), s_{jj}^{*D} are elastic compliances at electric displacement D = constant. ECFs k_{31}^* (proportional to the piezoelectric coefficient d_{31}^*) and k_{32}^* (proportional to d_{32}^*) are taken as absolute values in Eq. (8).

2.3. Components of composites

Our further evaluations of the effective properties and FOMs from Eqs. (2), (8)–(11) were carried out by using the full sets of experimental electromechanical constants [3, 6, 21–24] of the material components, see Table 1. Of specific interest are the domain-engineered relaxor-

ferroelectric SC components that exhibit a high piezoelectric activity. In Table 1 we show the electromechanical properties of the high-performance PMN–*x*PT and PZN–0.08PT SCs, where $0.28 \leq x \leq 0.33$. The PMN–0.33PT and PZN–0.08PT compositions listed in Table 1 are related to the morphotropic phase boundary in the well-known relaxor-ferroelectric solid solutions [25] with the perovskite-type structure. The PMN–*x*PT and PZN–0.08PT SCs poled along [001] of the perovskite unit cell are characterised by non-180° domain types, which are shown in the inset 1 of Fig. 1, and by large piezoelectric coefficients d_{3j} and ECF k_{33}. As follows from Table 1, the piezoelectric coefficient d_{33} exhibits a monotonic decrease on decreasing the molar concentration x from 0.33 to 0.28. A similar decrease of $|d_{31}|$ is observed in the same x range, see Table 1.

In contrast to the aforementioned relaxor-ferroelectric SCs, polyurethane is the piezo-passive component, i.e., $d_{ij} = 0$, as shown in Table 1. Below we now analyse the piezoelectric performance and modified FOMs of the 2–2-type composites based on the SCs shown in Table 1.

3. Piezoelectric properties, modified figures of merit and large anisotropy factors

3.1. Piezoelectric properties

Taking into account Eqs. (1) and (8), we can write the transmission coefficient $\lambda_{3j,m}^*$ in terms of the electromechanical constants involved in the $\| C^* \|$ matrix from Eq. (4). The relation

$$\lambda_{3j,m}^* = 2\{\varepsilon_{33}^{*\sigma} s_{jj}^{*E} - [\varepsilon_{33}^{*\sigma} s_{jj}^{*E} (\varepsilon_{33}^{*\sigma} s_{jj}^{*E} - (d_{3j}^*)^2)]^{1/2}\}(d_{3j}^*)^{-2} - 1 \qquad (12)$$

suggests that the transmission coefficient $\lambda_{3j,m}^*$ depends on the three forms of electromechanical constants. The piezoelectric coefficients d_{3j}^* influence both $\lambda_{3j,m}^*$ from Eq. (12) and the remaining FOMs from Eqs. (9)–(11) to a large extent. For instance, as $d_{3j}^* \rightarrow 0$ we approach an indefinite 0 / 0 ratio in Eq. (12), and $F_{3j}^{*\sigma} = 0$ and $F_{3j}^{*\xi} = 0$ in accordance with Eqs. (10) and (11), respectively. An increase of $|d_{3j}^*|$ of the composite leads to appreciable changes in the behaviour of its modified FOMs.

In the case of 2–2-type composites based on the domain-engineered SCs, we consider three different volume-fraction (m) dependences of the piezoelectric coefficients d_{3j}^*, see Fig. 2. These composites are characterised by the macroscopic *mm*2 symmetry due to the presence of the SC component from the 4*mm* symmetry class [3, 21–24] and due to the number of interfaces between the SC and polymer layers, x_1 = constant, see Fig. 1. The smaller $|d_{31}^*|$ values at m = constant are due to the influence of interfaces that separate the highly piezo-active SC and piezo-passive polymer (monolithic or porous) components. The large d_{33}^* values at m = constant are

achieved as a result of the large $d_{33}^{(1)}$ of the SC component that is distributed continuously along the OX_3 axis, see Fig. 1.

The shape of the $d_{3j}^*(m)$ curves undergoes minor changes when replacing the monolithic polymer layers with the porous layers where the aspect ratio $\rho_p \leq 1$, compare Fig. 2, a–c. However, a change in the $d_{3j}^*(m)$ dependence is observed in the presence of a porous polymer with a system of highly oblate pores ($\rho_p >> 1$), see Fig. 2, d. This is a result of the change in the elastic properties of the porous polymer layer at $\rho_p >> 1$: in this case the elastic compliance $s_{33}^{(3\text{-}0)}$ becomes relatively large in comparison to $s_{11}^{(3\text{-}0)}$ of the porous layer. Such an elastic anisotropy of the porous layer leads to appreciable changes in the $d_{3j}^*(m)$ curves at relatively small volume fractions of SC m, i.e., in the volume-fraction range where the elastic properties of the porous polymer layer have an important role and strongly influences the effective piezoelectric properties of the composite. Moreover, the system of highly oblate pores in the polymer medium leads to a larger anisotropy of d_{3j}^* of the 2–2–0 composite in comparison to the anisotropy of d_{3j}^* of the similar 2–2 composite. It should be added that the similar $d_{3j}^*(m)$ curves are obtained for the 2–2 and 2–2–0 composites based on PZN–0.08PT.

3.2. Modified figures of merit

3.2.1. 2–2 connectivity

Examples of the volume-fraction (m) behaviour of the twelve modified FOMs of the 2–2 PMN–0.33PT-based composite are shown in Fig. 3, a–d, and further examples of the volume-fraction behaviour of the modified FOMs of the 2–2 PZN–0.08PT-based composite are shown in Fig. 3, e and f. Hereby we see that the modified FOMs of the studied 2–2 composites exhibit either non-monotonic or monotonic volume-fraction behaviour. Despite the intriguing dependence of the transmission coefficient $\lambda_{3j,m}^*$ on the piezoelectric coefficients d_{3j}^* [see Eq. (12)], we observe a similarity of the $\lambda_{3j,m}^*(m)$ (Fig. 3, a) and $d_{3j}^*(m)$ curves (Fig, 2). A transition from $\lambda_{3j,m}^*$ to L_{3j}^* in accordance with Eq. (9) does not lead to significant changes to the shape of the $L_{3j}^*(m)$ curves, cf. Fig. 3, a and Fig. 3, b. A mutual arrangement of the curves related to the piezoelectric effect (d_{3j}^* at j = 1, 2 and 3) does not lead to changes in Fig. 3, a ($\lambda_{3j,m}^*$ at j = 1, 2 and 3) and Fig. 3, b (L_{3j}^* at j = 1, 2 and 3). This is due to the fact that the monotonic character of the volume-fraction dependence of ECFs $k_{3j}^*(m)$ leads to a monotonic $L_{3j}^*(m)$ dependence. It should be added that differences between the $\lambda_{3j,m}^*(m)$ values related to the PZN–0.08PT-based and PMN–0.33PT-based composites are less than 10% in the wide m range, and therefore, in Fig. 3 we do not show the $\lambda_{3j,m}^*(m)$ dependence the PZN–0.08PT-based composite. Similarly, only a small difference is observed on comparing the $L_{3j}^*(m)$ values related to the PZN–0.08PT-based and PMN–0.33PT-based composites.

Important examples of the non-monotonic volume-fraction (m) behaviour of the modified FOMs $F_{3j}^{*\sigma}$ are shown in Fig. 3, c and e. The maxima of $F_{3j}^{*\sigma}$ in Fig. 3, c are a result of the link between $F_{3j}^{*\sigma}$ and $(Q_{3j}^{*})^2$ [see Eq. (10)] and max$[Q_{3j}^{*}(m)^2]$ at smaller volume fractions m. The smaller m values suggest that the dielectric properties of the composite strongly influence its FOMs $(Q_{3j}^{*})^2$. Based on Eqs. (2) and (10), we represent $F_{3j}^{*\sigma}$ in the form $F_{3j}^{*\sigma} = L_{3j}^{*} d_{3j}^{*} g_{3j}^{*}$, and using the relation [6, 19] between the piezoelectric coefficients $d_{3j}^{*} = \varepsilon_{33}^{*\sigma} g_{3j}^{*}$, we write $F_{3j}^{*\sigma}$ as follows:

$$F_{3j}^{*\sigma} = L_{3j}^{*} (d_{3j}^{*})^2 / \varepsilon_{33}^{*\sigma}, \quad (13)$$

where j = 1, 2 and 3. As is known from earlier studies on 2–2-type composites [6], at a volume fraction of SC $m << 1$ the piezoelectric coefficient $d_{33}^{*}(m)$ exhibits a larger increase in comparison to $\varepsilon_{33}^{*\sigma}(m)$. This leads to a maximum of $F_{33}^{*\sigma}(m)$ and large values of this modified FOM from Eq. (13). The smaller max$F_{31}^{*\sigma}$ and max$F_{32}^{*\sigma}$ values (see curves 1 and 2 in Fig. 3, c and e) are due to the smaller $|d_{31}^{*}|$ and $|d_{32}^{*}|$ values in comparison to d_{33}^{*}. Our comparison of max$F_{33}^{*\sigma}$ related to the studied 2–2 composites (see Fig. 3, c and e) shows that the largest max$F_{33}^{*\sigma}$ value is achieved for the PMN–0.33PT-based composite, which is observed at a small volume fraction m (see curve 3 in Fig. 3, c), and the piezoelectric coefficient d_{33}^{*} in this m region approaches 1000 pC / N (see curve 3 in Fig. 2, a). The small volume fraction m leads to a lower dielectric permittivity $\varepsilon_{33}^{*\sigma}$ and, according to Eq. (13), leads to the large modified FOM $F_{33}^{*\sigma}$. We add that L_{33}^{*} at m = constant (see curve 3 in Fig. 3, b) undergoes minor changes after replacing the PMN–0.33PT SC with the PZN–0.08PT SC in the composite, and a difference between the ECF $k_{33}^{(1)}$ values of these SCs [3, 24] does not exceed 3%.

In contrast to the modified FOMs $F_{3j}^{*\sigma}$ from Fig. 3, c and e, the modified FOMs $F_{3j}^{*\xi}$ with j = 1, 2 and 3 exhibit a monotonic behaviour, see Fig. 3, d and f. This is likely to be due to the elastic compliances s_{jj}^{*E} and s_{jj}^{*D} of the composite [see Eq. (11)], which are interrelated [19] as follows: $s_{jj}^{*D} = s_{jj}^{*E}[1 - (k_{3j}^{*})^2] = s_{jj}^{*E} - (d_{3j}^{*})^2(\varepsilon_{33}^{*\sigma})^{-1}$, where j = 1, 2 and 3. The graphs in Fig. 3, d and f indicates that the PMN-0.33PT-based composite exhibits the largest FOMs $F_{3j}^{*\xi}$, especially at $m > 0.5$, and this high-performance is achieved due to the larger FOM $F_{3j}^{(1),\xi}$ of the SC component. The larger $F_{3j}^{(1),\xi}$ values of the PMN–0.33PT SC are related to the smaller elastic compliances $|s_{pq}^{(1),E}|$ with pq = 11, 12, 13, and 33 (see Table 1) in comparison to $|s_{pq}^{(1),E}|$ of PZN–0.08PT. As follows from Fig. 3, d and f, the large anisotropy of $F_{3j}^{*\xi}$ is observed, so that the conditions

$$F_{33}^{*\xi} / F_{31}^{*\xi} >> 1 \text{ and } F_{33}^{*\xi} / F_{32}^{*\xi} >> 1 \quad (14)$$

are valid.

Figure 4 shows the maxima of two longitudinal FOMs, namely, max[$(Q_{33}^*)^2$] and max$F_{33}^{*\sigma}$ of the 2–2 PMN–*x*PT SC / polyurethane composite as a function of PT fraction, *x*. As follows from Eq. (10), $F_{33}^{*\sigma}$ and $(Q_{33}^*)^2$ are linked in accordance with the relation $F_{33}^{*\sigma} / (Q_{33}^*)^2 = L_{33}^*$, and the proportionality between both FOMs is clear when comparing both the diagrams from Fig. 4. This proportionality is due to a relatively small (< 0.1) difference between values of the volume fraction *m* at which max$F_{33}^{*\sigma}$ and max[$(Q_{33}^*)^2$] are achieved in each 2–2 composite based on PMN–*x*PT with $0.28 \le x \le 0.33$. For example, in the composite based on PMN–0.33PT, max$F_{33}^{*\sigma}$ (see curve 3 in Fig. 3, c) and max[$(Q_{33}^*)^2$] are observed at $m = 0.184$ and 0.109, respectively. In the composite based on PMN–0.30PT, max$F_{33}^{*\sigma}$ and max[$(Q_{33}^*)^2$] are observed at $m = 0.116$ and 0.078, respectively. The diagrams in Fig. 4 show that the monotonic increase of both max$F_{33}^{*\sigma}$ and max[$(Q_{33}^*)^2$] with increasing *x* is consistent with the increase of the piezoelectric coefficient $d_{33}^{(1)}$ of the PMN–*x*PT SC in the same *x* range, see Table 1.

Table 2 shows the performance of the 2–2 PMN–*x*PT SC / polyurethane composite at volume fractions of SC $m = 0.1$ and 0.2. These *m* values are of interest due to their proximity to the volume fractions related to the aforementioned max$F_{33}^{*\sigma}$ and max[$(Q_{33}^*)^2$]. We see the consistent increase of FOMs $F_{3j}^{*\sigma}$ and $(Q_{3j}^*)^2$ on increasing *x* at *m* = constant. A similar consistent increase of FOMs is observed in a 1–3 PMN–*x*PT SC / polyurethane composite [26] wherein the SC component is represented by the parallelepiped-shaped rods that are parallel to the poling axis OX_3. In contrast to changes in d_{3j}^*, $(Q_{3j}^*)^2$ and $F_{3j}^{*\sigma}$ of the 2–2 composite on increasing *x* at *m* = constant, the modified FOMs $\lambda_{3j,m}^*$, L_{3j}^* and $F_{3j}^{*\xi}$ show smaller changes (see Table 2). This is a result of the influence of the elastic properties of the SC component on $\lambda_{3j,m}^*$, L_{3j}^* and $F_{3j}^{*\xi}$ of the 2–2 composite. The elastic properties of the PMN–*x*PT SC vary in a relatively narrow range, see Table 1, and the volume fractions of SC $m = 0.1$ and 0.2 are relatively small and do not strongly influence the elastic properties of the studied 2–2 composite. It should be noted that conditions (14) are valid at $m = 0.1$ and 0.2 irrespective of *x*, see Table 2. The largest $F_{33}^{*\xi}$ value at $m = 0.2$ is achieved in the PMN–0.28PT-based composite SC due to the smallest elastic compliance $s_{33}^{(1),E}$ of this SC, among those listed in Table 2.

3.2.2. 2–2–0 connectivity

The influence of porosity on the modified FOMs from Eqs. (8)–(11) is shown in Fig. 5. Hereby we consider 2–2–0 composites whereby air pores are characterised by one of the following aspect ratios: $\rho_p = 0.01$ (highly prolate pores), $\rho_p = 1$ (spherical pores), or $\rho_p = 100$ (highly oblate pores). It is seen that in the porosity range of $0 < m_p \le 0.3$, irrespective of the SC component, the modified FOMs $\lambda_{3j,m}^*$ and L_{3j}^* only undergo minor changes (see Fig. 5, a, c , e, and g) with the

exception of $\lambda_{31,m}^*$, $\lambda_{33,m}^*$ and L_{33}^* at $\rho_p = 100$ (see curves 1, 3 and 6 in Fig. 5, e and g). The graphs in Fig. 5, b, d, f, and h suggest that the modified FOMs $F_{3j}^{*\sigma}$ and $F_{3j}^{*\xi}$ undergo appreciable changes at various aspect ratios ρ_p, and we observe a validity of conditions (14) in the wide ρ_p range and validity of inequalities

$$F_{33}^{*\sigma} / F_{31}^{*\sigma} >> 1 \text{ and } F_{33}^{*\sigma} / F_{32}^{*\sigma} >> 1 \quad (15)$$

at $\rho_p = 100$. It should be noted that the graphs in Fig. 5 are related to 2–2–0 composites at $m = 0.1$, where the volume fraction of the porous polymer layers $1 - m$ is nine times larger than the volume fraction of the SC layers m. The value of $m = 0.1$ is of specific interest because $\max F_{33}^{*\sigma}$ can be found in the vicinity of this volume fraction, as follows, for instance, from Table 3.

Table 3 shows that an increase in $\max F_{33}^{*\sigma}$ values is observed on increasing porosity m_p and/or aspect ratio ρ_p. These factors lead to an appreciable decrease of the volume fraction of SC m_3 (that is related to $\max F_{33}^{*\sigma}$), and therefore, a decrease of the dielectric permittivity $\varepsilon_{33}^{*\sigma}$ of the composite. This takes place in the region of $m << 1$, where the piezoelectric coefficient d_{33}^* of the composite increases rapidly (see, e.g., curve 3 in Fig. 2, b–d). The porous polymer layers at $\rho_p >> 1$ lead to a large anisotropy of $F_{3j}^{*\sigma}$: for instance, at $\rho_p = 100$ we observe a validity of conditions (15) in a wide m_p range (see Table 3). It is of interest to note that the difference between the $\max F_{33}^{*\sigma}$ values of the PMN–0.33PT-based and PZN–0.08PT-based composites at m_p = constant and ρ_p = constant remains relatively small, irrespective of the pore shape.

In Fig. 6 we show the volume-fraction (m) behaviour of the modified FOMs of the 2–2–0 composite that contains the porous polymer layers with $\rho_p >> 1$. We focus our attention here on the modified FOMs concerned with the longitudinal piezoelectric effect and note the large anisotropy of the transmission coefficients $\lambda_{3j,m}^*$, i.e., the conditions

$$\lambda_{33,m}^* / \lambda_{31,m}^* >> 1 \text{ and } \lambda_{33,m}^* / \lambda_{32,m}^* >> 1 \quad (16)$$

hold in a wide m range at porosity $m_p = 0.1 - 0.3$ in each polymer layer. On comparing the graphs in Fig. 6, a, c and e, we see minor changes of the $\lambda_{33,m}^*(m)$ and $L_{3j}^*(m)$ dependences on increasing the fraction of porosity m_p from 0.1 to 0.3. As follows from Fig. 6, b, d and f, the $\max F_{33}^{*\sigma}(m)$ increases and shifts towards the smaller volume fraction of SC m on increasing the porosity m_p, and the $F_{33}^{*\xi}(m)$ dependence undergoes minor changes in the same m and m_p ranges. The trends of the $\max F_{33}^{*\sigma}(m)$ behaviour (see Fig. 6, b, d and f) are similar to those shown for the PZN–0.08PT-based composite in Table 3. The modified FOMs $F_{33}^{*\sigma}$ and $F_{33}^{*\xi}$ of the PMN–0.33PT-based and PZN–0.08PT-based composites at the aspect ratio $\rho_p >> 1$ obey conditions (14) and (15) for a large anisotropy.

Table 4 shows the linkages between the modified FOMs $F_{3j}^{*\sigma}$ and FOMs $(Q_{3j}^{*})^2$ of the 2–2–0 PMN–0.33PT-based composite at $\rho_p >> 1$. We observe a similar volume-fraction (m) behaviour of these FOMs and their large values at $m << 1$. Hereby we emphasise the strong influence of the relatively small dielectric permittivity $\varepsilon_{33}^{*\sigma}$ on both $F_{3j}^{*\sigma}$ and $(Q_{3j}^{*})^2$ in accordance with Eq. (13) and the formula $(Q_{3j}^{*})^2 = (d_{3j}^{*})^2 / \varepsilon_{33}^{*\sigma}$. The modified FOM $F_{33}^{*\sigma}$ concerned with the longitudinal piezoelectric effect has a maximum at a volume fraction m_3 that is larger than a volume fraction related to $\max[(Q_{33}^{*})^2]$, which has an important implication on piezotechnical stress-driven systems. Table 4 suggests that conditions (15) and

$$(Q_{33}^{*})^2 / (Q_{31}^{*})^2 >> 1 \text{ and } (Q_{33}^{*})^2 / (Q_{32}^{*})^2 >> 1 \quad (17)$$

hold in wide m ranges.

3.3. Diagrams on a large anisotropy of modified figures of merit

Validity of conditions (14)–(17) for a large anisotropy of the studied FOMs means the high effectiveness of the energy conversion in the composite sample (see Fig. 1) along the OX_3 axis in comparison to the energy conversion along the OX_1 or OX_2 axis. In Fig. 7 we present new diagrams to show the volume-fraction (m and m_p) ranges where a large anisotropy of two modified FOMs is achieved. Both diagrams in Fig. 7 are related to 2–2–0 composites with aspect ratio of pores $\rho_p >> 1$. These diagrams suggest that conditions for the large anisotropy

$$F_{33}^{*\sigma} / F_{31}^{*\sigma} > 10 \text{ and } \lambda_{33,m}^{*} / \lambda_{31,m}^{*} > 10 \quad (18)$$

hold simultaneously in a wide m range, while conditions

$$F_{33}^{*\sigma} / F_{32}^{*\sigma} > 10 \text{ and } \lambda_{33,m}^{*} / \lambda_{32,m}^{*} > 10 \quad (19)$$

are valid simultaneously in a relatively narrow m range, at $m << 1$. The reason of this distinction is related with three features of a piezoelectric response of the 2–2–0 composite as follows.

Firstly, the system of interfaces x_1 = constant in the composite in Fig. 1 leads to a weakening of the piezoelectric effect related to d_{31}^{*}. Secondly, the system of pores at $\rho_p >> 1$ in each polymer layer leads to a stronger piezoelectric effect related to d_{33}^{*}, even at a volume fraction of SC $m << 1$. Thirdly, changes in porosity m_p from 0.1 to 0.3 do not lead to drastic changes of the diagram areas where the conditions (18) and (19) valid. This is illustrated by minor changes of the length of arrows 1–4 on varying the m_p value, see Fig. 7. In fact, the highly oblate shape of the pore in the polymer layer plays an important role in forming the large anisotropy of the modified FOMs (18) and (19), irrespective of the SC component (cf. Fig. 7, a and Fig. 7, b). As is known from Table 1, the SC components are characterised by a moderate anisotropy of the piezoelectric coefficients d_{3j} and, therefore, cannot be responsible for the validity of conditions (18) and (19) for the composite, especially at $m << 1$.

4. Comparison and discussion

In Table 5 we show the ECFs and modified FOMs of 2–2–0 composites at three volume fractions of SC, namely, at m = 0.2 (SC has only a moderate influence), m = 0.5 (equal volume fractions of the SC and porous polymer layers), and m = 0.7 (SC has a strong influence). We compare the aforementioned parameters of the PMN–0.33PT-based and PZN–0.08PT-based composites. It is shown that the larger ECF k_{33}^* of the PMN–0.33PT-based composite leads to larger modified FOMs $\lambda_{33,m}^*$, L_{33}^*, $F_{33}^{*\sigma}$, and $F_{33}^{*\xi}$, which are related to the longitudinal piezoelectric effect. This trend is observed at a variety of volume fractions m, from 0.2 to 0.7 (see Table 5). We note that the larger piezoelectric coefficient d_{33} of the PZN–0.08PT SC in comparison to the d_{33} of the PMN–0.33PT SC (see Table 1) cannot simply promote a larger $\lambda_{33,m}^*$, L_{33}^*, $F_{33}^{*\sigma}$, and $F_{33}^{*\xi}$ values in a specific m range. This is due to the influence of the porous polymer layers of the composite on its piezoelectric performance, ECFs and FOMs, and such an influence should be taken into consideration even, for instance, at a large volume fraction of SC m = 0.7.

The studied composites are of interest due to the large values of the modified FOMs $\lambda_{33,m}^*$, L_{33}^*, $F_{33}^{*\sigma}$, and $F_{33}^{*\xi}$ and due to the large anisotropy of the FOMs, see validity of conditions (14)–(17). The values of $\lambda_{33,m}^*$, L_{33}^*, $F_{33}^{*\sigma}$, and $F_{33}^{*\xi}$ in a wide m range are comparable to those of a poled porous ferroelectric $BaTiO_3$ ceramic [9], although the max$F_{33}^{*\sigma}$ values (see Fig. 6, b, d and f, and Table 3) are larger than the typical $F_{33}^{*\sigma}$ values of the porous $BaTiO_3$ ceramic from this previous work. It should be noted, however, that the piezoelectric d_{3j} coefficients of the poled monolithic $BaTiO_3$ ceramic are an order-of-magnitude lower [6] than the d_{3j} values of the SC-based composites studied here.

On comparing the ECFs k_{3j}^* from Eq. (1) and transmission coefficients $\lambda_{3j,m}^*$ from Eq. (8), we demonstrate that the larger $\lambda_{33,m}^*$ value is achieved at a larger k_{33}^* value, see Table 6. However a large anisotropy of $\lambda_{3j,m}^*$ is observed in the volume-fraction region where the anisotropy of the ECFs k_{3j}^* remains moderate. A difference between the anisotropy factors concerned with $\lambda_{3j,m}^*$ and k_{3j}^* is accounted for by the anisotropic elastic properties of the studied 2–2-type composites. We add that in these composites, an appreciable elastic anisotropy is achieved due to the system of the interfaces between the SC and polymer layers and due to the porous structure in the polymer layers, see Fig. 1.

A further comparison can be drawn by considering data from Table 6 and work [27–31]. Prior to the publication of work [9, 19] on modified FOMs (8)–(11), a number of authors have used the ECFs k_{3j}^* to evaluate the effectiveness of piezo-active composites in energy-harvesting [6] and other applications. Taking the k_{3j}^* values from work [27–31] and using Eqs. (8) and (9),

we evaluate the modified FOMs $\lambda_{3j,m}^*$ and L_{3j}^* for specific piezo-active composites, as shown in the 3rd and 4th columns in Table 6. As follows from Table 6, the $\lambda_{33,m}^*$ and L_{33}^* values of the 1–3-type PMN–0.33PT-based composite studied in work [27] are approximately equal to the related FOMs of the 2–2 PMN–0.33PT SC / polyurethane composite at $m > 0.5$ (see curve 3 in Fig. 3, a and b). Moreover, the $\lambda_{33,m}^*$ and L_{33}^* values of the related 2–2–0 PMN–0.33PT SC / porous polyurethane composite at $m = 0.1$, $m_p = 0.2$–0.3 and $\rho_p = 100$ differ from the similar FOMs of the 1–3-type PMN–0.33PT-based composite to a small degree.

The results on 1–3 and 2–2 composites show that the modified FOMs from the 3rd and 4th columns of Table 6 are comparable to the similar parameters of the 2–2-type composites from our present study, see, e.g. Figs. 3, a and b, and 5, a, c, e, and g.

5. Conclusions

This paper reports new results on the twelve modified figures of merit (FOMs), given in Eqs. (8)–(11), which are concerned with the longitudinal (ij = 33) or lateral (ij = 31 and 32) piezoelectric effect in the parallel-connected 2–2 and 2–2–0 composites based on domain-engineered relaxor-ferroelectric SCs. This has been the first study on the vast group of the FOMs in composites whereby differences between their piezoelectric coefficients d_{3j}^* are observed (Fig. 2) in a wide volume-fraction (m) range and with changes in the volume fraction m_p and aspect ratio ρ_p of pores in the polymer layers. In addition to electromechanical coupling factors, [Eq. (1)] and traditional (squared) FOMs [Eq. (2)], which strongly depend on d_{3j}^*, the new modified FOMs from Eqs. (8)–(11) are taken into account to evaluate the effectiveness of piezo-active composites for energy conversion, energy harvesting and under external mechanical fields (either at σ = constant or ξ = constant). In the present study we demonstrate the influence of the relaxor-ferroelectric SC component with high piezoelectric activity and the influence of porosity of the piezo-passive polymer medium on the modified FOMs and their anisotropy.

Our results on the modified FOMs (see Figs. 3–6 and Table 3) show that the studied parameters vary in wide ranges. A highly oblate pore shape ($\rho_p >> 1$) is preferable to achieve a larger longitudinal piezoelectric coefficient d_{33}^* at a smaller volume fraction of SC m and, as a consequence, to achieve larger values of the modified FOMs, in particular $F_{33}^{*\sigma}$. The porous structure of the polymer layers leads to a large anisotropy of the modified FOMs, and conditions (14)–(16) hold in specific volume-fraction (m and m_p) ranges. The important relationship between the traditional (squared) FOMs $(Q_{3j}^*)^2$ and modified FOMs $F_{3j}^{*\sigma}$ [see Eq. (10) and Table 4] is to be taken into account in the context of the large anisotropy of FOMs and further applications of piezo-active composites. The obvious advantage of the $F_{33}^{*\sigma}(m)$ dependence (see

Fig. 3, c and e) over the $[Q_{33}^{*}(m)]^2$ dependence of many piezo-active composites [6] consists in the presence of $\max F_{33}^{*\sigma}(m)$ at a larger volume fraction of SC m, and this can facilitate the manufacture of such 2–2-type composites. This advantage is due to the strong influence of the ECFs on the $F_{33}^{*\sigma}(m)$ behaviour, see Eqs. (8)–(10). The new diagrams presented in Fig. 7 suggest that both the PMN–0.33PT-based and PZN–0.08PT-based composites are of value as advanced piezoelectric materials with a large anisotropy of two kinds of the modified FOMs, namely, $F_{3j}^{*\sigma}$ and $\lambda_{3j,m}^{*}$, for which conditions (18) and (19) hold simultaneously. Moreover, the modified FOMs $\lambda_{3j,m}^{*}$ and L_{3j}^{*} of the studied 2–2-type composites are either larger or approximately equal to the similar FOMs of the composites listed in Table 6.

The large modified FOMs $\lambda_{33,m}^{*}$, L_{33}^{*}, $F_{33}^{*\sigma}$, and $F_{33}^{*\xi}$ of the 2–2-type composites based on relaxor-ferroelectric SCs are to be taken into account in a variety of piezotechnical applications including transducers based on stress-driven and strain-driven systems, where energy conversion and harvesting play the key role and where the longitudinal mode can be exploited due to the large anisotropy of specific FOMs.

Acknowledgements

The authors would like to thank Prof. Dr. A.A. Nesterov, Prof. Dr. A.E. Panich and Prof. Dr. I.A. Parinov (Southern Federal University, Russia), and Prof. Dr. S.-H. Chang (National Kaohsiung University of Science and Technology, Taiwan, ROC) for their research interest in the field of advanced piezoelectric materials. Research was financially supported by Southern Federal University, grant No. VnGr-07/2020-04-IM (Ministry of Science and Higher Education of the Russian Federation). CRB acknowledges the Leverhulme Trust (RGP-2018-290).

References

[1] T. Ritter, X. Geng, K.K. Shung, P.D. Lopath, S.-E. Park, T.R. Shrout, Single crystal PZN/PT-polymer composites for ultrasound transducer applications, IEEE Trans. Ultrason., Ferroelectr., Freq. Control 47 (2000) 792–800. DOI: 10.1109/58.852060

[2] F. Wang, C. He, Y. Tang, Single crystal 0.7Pb($Mg_{1/3}Nb_{2/3}$)O_3–0.3$PbTiO_3$ / epoxy 1–3 piezoelectric composites prepared by the lamination technique, Mater. Chem. Phys. 105 (2007) 273–277. DOI: 10.1016/j.matchemphys.2007.04.060

[3] R. Zhang, B. Jiang, W. Cao, Elastic, piezoelectric, and dielectric properties of multidomain 0.67Pb($Mg_{1/3}Nb_{2/3}$)O_3–0.33$PbTiO_3$ single crystals, J. Appl. Phys. 90 (2001) 3471–3475. DOI: 10.1063/1.1390494

[4] S. Zhang, F. Li, X. Jiang, J. Kim, J. Luo, X. Geng, Advantages and challenges of relaxor-$PbTiO_3$ ferroelectric crystals for electroacoustic transducers – A review, Progress in Materials Science 68 (2015) 1–66. DOI: 10.1016/j.pmatsci.2014.10.002

[5] K. Ren, Y. Liu, X. Geng, H.F. Hofmann, Q.M. Zhang, Single crystal PMN–PT/epoxy 1–3 composite for energy-harvesting application, IEEE Trans. Ultrason., Ferroelectr., Freq. Control 53 (2006) 631–638. DOI: 10.1109/TUFFC.2006.1610572

[6] C.R. Bowen, V.Yu. Topolov, H.A. Kim, Modern Piezoelectric Energy Harvesting, Springer International Publ. Switzerland, Cham, 2016.

[7] K. Uchino, Piezoelectric energy harvesting systems – Essentials to successful developments, Energy Technol. 6 (2018) 829–848. https://doi.org/10.1002/ente.201700785

[8] P.A. Borzov, V.Yu. Topolov, C.R. Bowen, Relations between the piezoelectric performance and quality factors in a corundum-containing composite, Mater. Chem. Phys. 233 (2019) 194–202. https://doi.org/10.1016/j.matchemphys.2019.05.019

[9] J.I. Roscow, H. Pearce, H. Khanbareh, S. Kar-Narayan, C.R. Bowen, Modified energy harvesting figures of merit for stress- and strain-driven piezoelectric systems, Eur. Phys. J. Spec. Topics 228 (2019) 1537–1554. https://doi.org/10.1140/epjst/e2019-800143-7

[10] A.A. Nesterov, E.A. Panich, Technology and electrophysical parameters of piezocomposites with a connection type 2–0–2, Springer Proc. Phys. 224 (2019) 95–101. DOI: 10.1007/978-3-030-19894-7_8

[11] A.A. Nesterov, V.Yu. Topolov, M.I. Tolstunov, A.N. Isaeva, Longitudinal piezoelectric effect and hydrostatic response in novel laminar composites based on ferroelectric ceramics, Ceram. Internat. 45 (2019) 22241–22248. DOI: 10.1016/j.ceramint.2019.07.248

[12] Z. Zeng, L. Gai, A. Petitpas, Y. Li, H. Luo, D. Wang, X. Zhao, A flexible, sandwich structure piezoelectric energy harvester using PIN-PMN-PT/epoxy 2-2 composite flake for wearable application, Sens. Actuat. A – Phys. 265 (2017) 62–69. DOI: 10.1016/j.sna.2017.07.059
[13] B. Mahanty, S. K. Ghosh, S. Garain, D. Mandal, An effective flexible wireless energy harvester/sensor based on porous electret piezoelectric polymer, Mater. Chem. Phys. 186 (2017) 327–332. DOI: 10.1016/j.matchemphys.2016.11.003
[14] A. Pal, A. Sasmal, B. Manoj, D.P. Rao, A.K. Haldar, S. Sen, Enhancement in energy storage and piezoelectric performance of three phase (PZT/MWCNT/PVDF) composite, Mater. Chem. Phys. 244 (2020) 122639. https://doi.org/10.1016/j.matchemphys.2020.122639
[15] R.E. Newnham, D.P. Skinner, L.E. Cross, Connectivity and piezoelectric-pyroelectric composites, Mater. Res. Bull. 13 (1978) 525–536. DOI: 10.1016/0025-5408(78)90161-7
[16] F. Levassort, M. Lethiecq, C. Millar, L. Pourcelot, Modeling of highly loaded 0–3 piezoelectric composites using a matrix method, IEEE Trans. Ultrason., Ferroelectr., Freq. Control 45 (1998) 1497–1505. DOI: 10.1109/58.738289
[17] J.H. Huang, W.-S. Kuo, Micromechanics determination of the effective properties of piezoelectric composites containing spatially oriented short fibers, Acta Mater. 44 (1996) 4889–4898. DOI: 10.1016/S1359-6454(96)00090-0
[18] M.L. Dunn, M. Taya, Electromechanical properties of porous piezoelectric ceramics, J. Am. Ceram. Soc. 76 (1993) 1697–1706. DOI: 10.1111/j.1151-2916.1993.tb06637.x
[19] T. Ikeda, Fundamentals of Piezoelectricity. Oxford University Press, Oxford, New York, Toronto, 1990.
[20] D.B. Deutz, J.-A. Pascoe, B. Schelen, S. van der Zwaag, D. M. de Leeuw, P. Groen, Analysis and experimental validation of the figure of merit for piezoelectric energy harvesters, Mater. Horiz. 5 (2018) 444–453. https://doi.org/10.1039/C8MH00097B
[21] R. Zhang, W. Jiang, B. Jiang, W. Cao, Elastic, dielectric and piezoelectric coefficients of domain engineered $0.70Pb(Mg_{1/3}Nb_{2/3})O_3–0.30PbTiO_3$ single crystal. *Fundamental Physics of Ferroelectrics*, ed. by R.E. Cohen (American Institute of Physics, Melville, 2002) p. 188–197.
[22] S. Zhang, J. Luo, W. Hackenberger, T.R. Shrout, Characterization of $Pb(In_{1/2}Nb_{1/2})O_3–Pb(Mg_{1/3}Nb_{2/3})O_3–PbTiO_3$ ferroelectric crystal with enhanced phase transition temperatures J. Appl. Phys. 104 (2008) 064106. DOI: 10.1063/1.2978333
[23] G. Liu, W. Jiang, J. Zhu, W. Cao, Electromechanical properties and anisotropy of single and multi-domain $0.72Pb(Mg_{1/3}Nb_{2/3})O_3–0.28PbTiO_3$ single crystals. Appl. Phys. Lett. 99 (2011) 162901. DOI: 10.1063/1.3652703

[24] R. Zhang, B. Jiang, W. Cao, A. Amin, Complete set of material constants of 0.93Pb($Zn_{1/3}Nb_{2/3}$)O_3-0.07$PbTiO_3$ domain engineered single crystal, J. Mater, Sci. Lett. 21 (2002) 1877–1879. https://doi.org/10.1023/A:1021573431692

[25] B. Noheda, Structure and high-piezoelectricity in lead oxide solid solutions, Curr. Opin. Solid State Mater. Sci. 6 (2002) 27–39. https://doi.org/10.1016/S1359-0286(02)00015-3

[26] V.Yu. Topolov, A.N. Isaeva, Modified reception parameters of 1–3 composites based on ferroelectric crystals, Technical Physics 66 (2021) 938–948. doi: 10.1134/S1063784221060207

[27] S.V. Bezus, V.Yu. Topolov, C.R. Bowen, High-performance 1–3-type composites based on $(1-x)$Pb($A_{1/3}$ $Nb_{2/3}$)O_3–$x$$PbTiO_3$ single crystals (A = Mg, Zn). J. Phys. D: Appl. Phys. 39 (2006) 1919–1925. doi:10.1088/0022-3727/39/9/029

[28] H.J. Lee, S.J. Zhang, T.R. Shrout, Scaling effects of relaxor-$PbTiO_3$ crystals and composites for high frequency ultrasound, J. Appl. Phys. 107 (2010) 124107. https://aip.scitation.org/doi/10.1063/1.3437068

[29] S. Zhang, F. Li, X. Jiang, J. Kim, J. Luo, X. Geng, Advantages and challenges of relaxor-$PbTiO_3$ ferroelectric crystals for electroacoustic transducers – A review, Progr. Mater. Sci. 68 (2015) 1–66. http://dx.doi.org/10.1016/j.pmatsci.2014.10.002

[30] S. Zhang, F. Li, High performance ferroelectric relaxor-$PbTiO_3$ single crystals: Status and perspective, J. Appl. Phys. 111 (2012) 031301. http://dx.doi.org/10.1063/1.3679521

[31] J. Sun, P. Ngernchuklin, M. Vittadello, E.K. Akdoğan, A. Safari, Development of 2–2 piezoelectric ceramic/polymer composites by direct-write technique, J. Electroceram. 24 (2010) 219–225. DOI 10.1007/s10832-009-9561-3

Table 1. Room-temperature elastic compliances s_{ab}^{E} (in 10^{-12} Pa^{-1}), piezoelectric coefficients d_{ij} (in pC / N) and dielectric permittivities $\varepsilon_{pp}^{\sigma}$ of components

Components	s_{11}^{E}	s_{12}^{E}	s_{13}^{E}	s_{33}^{E}	s_{44}^{E}	s_{66}^{E}	d_{31}	d_{33}	d_{15}	$\varepsilon_{11}^{\sigma}/\varepsilon_0$	$\varepsilon_{33}^{\sigma}/\varepsilon_0$
PMN–0.33PT SC[a] [3]	69.0	–11.1	–55.7	119.6	14.5	15.2	–1330	2820	146	1600	8200
PMN–0.30PT SC[a] [21]	52.0	–18.9	–31.1	67.7	14.0	15.2	–921	1981	190	3600	7800
PMN–0.29PT SC[a] [22]	52.1	–24.6	–26.4	59.9	16.0	28.3	–699	1540	164	1560	5400
PMN–0.28PT SC[a] [23]	44.57	–28.91	–13.91	34.38	15.22	16.34	–569	1182	122	1672	5479
PZN–0.08PT SC[a] [24]	87.0	–13.1	–70.0	141	15.8	15.4	–1455	2890	158	2900	7700
Polyurethane [6]	405	–151	–151	405	1110	1110	0	0	0	3.5	3.5

[a] Domain-engineered SC poled along [001] of the perovskite unit cell, macroscopic 4*mm* symmetry. See the schematic of domains in inset 1 on Fig. 1

Table 2. Piezoelectric coefficients d_{3j}^* (in pC/ N) and FOMs $(Q_{3j}^*)^2$ (in 10^{-12} Pa^{-1}), $\lambda_{3j,m}^*$, L_{3j}^*, $F_{3j}^{*\sigma}$ (in 10^{-12} Pa^{-1}), and $F_{3j}^{*\xi}$ (in 10^{10} Pa) of the 2–2 PMN–*x*PT SC / polyurethane composite at m = 0.1 and 0.2

x	0.33	0.33	0.30	0.30	0.29	0.29	0.28	0.28
m	0.1	0.2	0.1	0.2	0.1	0.2	0.1	0.2
d_{33}^*	768	1290	789	1180	659	966	669	882
d_{32}^*	–328	–571	–334	–521	–278	–419	–305	–411
d_{31}^*	–277	–472	–284	–433	–238	–354	–236	–320
$(Q_{33}^*)^2$	241	217	181	153	171	141	144	102
$(Q_{32}^*)^2$	44.0	44.6	32.5	29.6	30.3	26.5	30.1	22.1
$(Q_{31}^*)^2$	31.3	30.4	23.4	20.4	22.3	18.9	17.9	13.4
$\lambda_{33,m}^*$	0.343	0.417	0.271	0.339	0.268	0.332	0.326	0.375
$\lambda_{32,m}^*$	0.0462	0.0646	0.0366	0.0479	0.0337	0.0419	0.0361	0.0385
$\lambda_{31,m}^*$	0.0253	0.0288	0.0194	0.0200	0.0184	0.0184	0.0151	0.0134
L_{33}^*	0.439	0.502	0.404	0.448	0.402	0.444	0.439	0.472
L_{32}^*	0.274	0.283	0.269	0.275	0.267	0.271	0.268	0.270
L_{31}^*	0.263	0.265	0.260	0.260	0.259	0.259	0.258	0.257
$F_{33}^{*\sigma}$	106	114	72.9	68.5	68.8	62.5	63.4	48.1
$F_{32}^{*\sigma}$	15.0	18.1	11.5	12.7	10.6	11.2	11.0	9.90
$F_{31}^{*\sigma}$	8.23	8.05	6.09	5.31	5.79	4.91	4.62	3.44
$F_{33}^{*\xi}$	0.383	0.899	0.304	0.685	0.313	0.705	0.646	1.41
$F_{32}^{*\xi}$	0.0171	0.0299	0.0135	0.0219	0.0122	0.0186	0.0136	0.0175
$F_{31}^{*\xi}$	0.00859	0.0115	0.00670	0.00819	0.00628	0.00743	0.00525	0.00549

Table 3. Local maxima of modified FOMs $F_{3j}{}^{*}\sigma$ (in 10^{-12} Pa^{-1}) and related anisotropy factors $F_{33}{}^{*}\sigma(m_3) / F_{31}{}^{*}\sigma(m_3)$ and $F_{33}{}^{*}\sigma(m_3) / F_{32}{}^{*}\sigma(m_3)$ of the 2–2–0 PZN–0.08PT SC / porous polyurethane composite[a] at ρ_p = constant and m_p = constant.

ρ_p	m_p	max$F_{33}{}^{*}\sigma$	m_3	$F_{33}{}^{*}\sigma(m_3) / F_{31}{}^{*}\sigma(m_3)$	$F_{33}{}^{*}\sigma(m_3) / F_{32}{}^{*}\sigma(m_3)$
0.01	0.1	101	0.232	12.6	4.50
	0.2	111	0.199	13.0	3.90
	0.3	124	0.169	13.3	3.42
1	0.1	109	0.206	13.7	5.30
	0.2	128	0.161	15.2	5.32
	0.3	153	0.126	16.8	5.36
100	0.1	458	0.025	777	76.1
	0.2	865	0.012	2790	197
	0.3	1350	0.008	5840	361

[a]The volume fraction of SC m_3 is found from the equation max$F_{33}{}^{*}\sigma = F_{33}{}^{*}\sigma(m_3)$ at ρ_p = constant and m_p = constant.

Table 4. Links between modified FOMs $F_{3j}^{*}\sigma$ (in 10^{-12} Pa^{-1}) and traditional FOMs $(Q_{3j}^{*})^2$ (in 10^{-12} Pa^{-1}) of the 2–2–0 PMN–0.33PT SC / porous polyurethane composite at ρ_p = 100, m_p = 0.3 and m = constant.

m / FOMs	0.05	0.10	0.15	0.30	0.50	0.70
$F_{31}^{*}\sigma$	0.0305	0.0124	$5.44 \cdot 10^{-3}$	0.0767	1.73	3.47
$F_{32}^{*}\sigma$	19.9	23.2	31,9	33.5	28.3	20/6
$F_{33}^{*}\sigma$	739	455	335	268	124	91.5
$(Q_{31}^{*})^2$	0.122	0.0496	0.0217	1.76	6.85	13.4
$(Q_{32}^{*})^2$	59.7	68.6	66.9	53/6	40.3	32.0
$(Q_{33}^{*})^2$	1370	808	585	327	208	153

Table 5. Comparison of effective parameters of the 2–0–2 PMN–0.33PT SC / porous polyurethane and PZN–0.08PT SC / porous polyurethane composites at ρ_p = 100, m_p = 0.3 and m = constant.

Effective parameters	PMN–0.33PT-based composite, m = 0.2	PZN–0.08PT-based composite, m = 0.2	PMN–0.33PT-based composite, m = 0.5	PZN–0.08PT-based composite, m = 0.5	PMN–0.33PT-based composite, m = 0.7	PZN–0.08PT-based composite, m = 0.7
k_{31}^*	–0.0268	–0.0379	–0.155	–0.174	–0.260	–0.285
k_{32}^*	–0.519	–0.506	–0.572	–0.570	–0.585	–0.585
k_{33}^*	0.950	0.919	0.955	0.928	0.956	0.931
$\lambda_{31,m}^*$	$1.79 \cdot 10^{-4}$	$3.59 \cdot 10^{-4}$	$6.06 \cdot 10^{-3}$	$7.65 \cdot 10^{-3}$	0.0175	0.0211
$\lambda_{32,m}^*$	0.0782	0.0739	0.0989	0.0980	0.104	0.105
$\lambda_{33,m}^*$	0.523	0.434	0.543	0.458	0.547	0.464
L_{31}^*	0.250	0.250	0.253	0.254	0.259	0.261
L_{32}^*	0.291	0.288	0.302	0.301	0.305	0.305
L_{33}^*	0.523	0.514	0.595	0.531	0.599	0.536
$F_{31}^{*\sigma}$, 10^{-12} Pa^{-1}	0.0767	0.156	1.73	2.27	3.47	4.48
$F_{32}^{*\sigma}$, 10^{-12} Pa^{-1}	33.5	32.2	28.3	29.1	20.6	22.1
$F_{33}^{*\sigma}$, 10^{-12} Pa^{-1}	268	252	124	121	91.5	90.9
$F_{31}^{*\xi}$, 10^{10} Pa	$4.18 \cdot 10^{-5}$	$8.23 \cdot 10^{-5}$	0.0217	$2.65 \cdot 10^{-3}$	$9.46 \cdot 10^{-3}$	0.0109
$F_{32}^{*\xi}$, 10^{10} Pa	0.0250	0.0228	0.0514	0.0489	0.0799	0.0751
$F_{33}^{*\xi}$, 10^{10} Pa	1.05	0.479	2.71	1.25	3.83	1.77

Table 6. ECFs of some piezo-active composites (published data) and evaluated modified FOMs $\lambda_{3j,m}^*$ and L_{3j}^* from Eqs. (8) and (9), respectively

Composites	k_{3j}^*	$\lambda_{3j,m}^*$	L_{3j}^*
1–3-type PMN–0.33PT SC / porous araldite composite at the volume fraction of SC m = 0.120 and aspect ratio of pores ρ_p = 100 [27]	$k_{33}^* = 0.946$	$\lambda_{33,m}^* = 0.510$	$L_{33}^* = 0.570$
1–3-type PMN–0.33PT SC / porous araldite composite at the volume fraction of SC m = 0.252 and aspect ratio of pores ρ_p = 10 [27]	$k_{33}^* = 0.941$	$\lambda_{33,m}^* = 0.494$	$L_{33}^* = 0.558$
1–3 PMN–xPT-based composites [28, 29], 2–2 PMN–xPT-based composites [30]	$k_{33}^* \approx 0.8$	$\lambda_{33,m}^* \approx 0.25$	$L_{33}^* \approx 0.39$
2–2 PZT ceramic / epoxy composite [31]	$k_{31}^* = -0.36$	$\lambda_{31,m}^* = 0.035$	$L_{31}^* = 0.27$

Figure captions to the paper "Twelve modified figures of merit of 2–2-type composites based on relaxor-ferroelectric single crystals" by A. N. Isaeva et al.

Fig. 1. Schematic of piezo-active parallel-connected 2–2-type composite. ($X_1X_2X_3$) is the rectangular co-ordinate system, m is the volume fraction of the SC layers, and 1 – m is the volume fraction of the polymer layers. In inset 1, spontaneous polarisation vectors $\boldsymbol{P}_{s,1}$, $\boldsymbol{P}_{s,2}$, $\boldsymbol{P}_{s,3}$, and $\boldsymbol{P}_{s,4}$ of domains in the SC layer are shown. In insets 2 and 3, polymer layers in the composite are characterised.

Fig. 2. Piezoelectric coefficients d_{3j}^* (in pC / N) of the 2–2-type composites based on the PMN–0.33PT SC: a, with the monolithic polyurethane layers, b – d, with the porous polyurethane layers (porosity m_p = 0.2) at the aspect ratio of pores ρ_p = 0.01 (b), 1 (c) and 100 (d).

Fig. 3. Volume-fraction (m) dependences of modified FOMs of the 2–2 PMN–0.33PT SC / polyurethane composite (a – d) and 2–2 PZN-0.08PT SC / polyurethane composite (e and f): a, $\lambda_{3j,m}^*$, b, L_{3j}^*, c and e, $F_{3j}^{*\sigma}$ (in 10^{-12} Pa^{-1}), and d and f, $F_{3j}^{*\xi}$ (in 10^{10} Pa).

Fig. 4. Diagrams of maximum values of FOMs $(Q_{33}^*)^2$ (a, in 10^{-12} Pa^{-1}) and $F_{3j}^{*\sigma}$ (b, in 10^{-12} Pa^{-1}) of the 2–2 PMN–xPT SC / polyurethane composite at $0.28 \le x \le 0.33$.

Fig. 5. Volume-fraction (m_p) dependences of modified FOMs of 2–2-type composites based on either the PMN–0.33PT SC (a – f) or PZN–0.08PT SC (g and h) at m = 0.1: a, c, e, and g, $\lambda_{3j,m}^*$ and L_{3j}^*, b, d, f, and h, $F_{3j}^{*\sigma}$ (in 10^{-12} Pa^{-1}), and $F_{3j}^{*\xi}$ (in 10^{10} Pa).

Fig. 6. Volume-fraction (m) dependences of modified FOMs of the 2–2–0 PMN–0.33PT SC / porous polyurethane composite at m_p = constant and ρ_p = 100: a, c and e, $\lambda_{3j,m}^*$ and L_{3j}^*, b, d and f, $F_{3j}^{*\sigma}$ (in 10^{-12} Pa^{-1}), and $F_{3j}^{*\xi}$ (in 10^{10} Pa).

Fig. 7. Diagrams showing the volume-fraction (m and m_p) areas wherein conditions for the large anisotropy of modified FOMs hold for the 2–2–0 PMN–0.33PT SC / porous polyurethane composite at ρ_p = 100 (graph a) and 2–2–0 PZN–0.08PT SC / porous polyurethane composite at ρ_p = 100 (graph b).

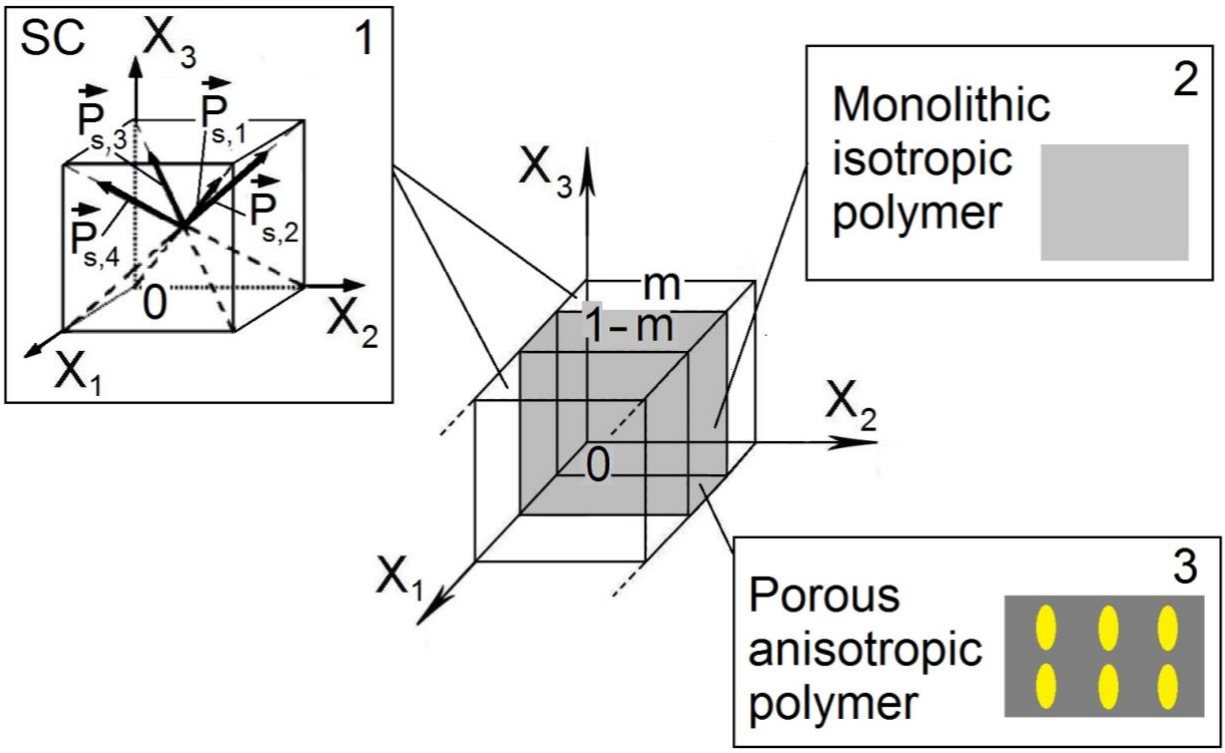
SC
X3
1
Ps,3
Ps,1
Ps,2
Ps,4
0
X2
X1
X3
m
1 – m
X2
0
X1
Monolithic
isotropic
polymer
2
Porous
anisotropic
polymer
3

Fig. 1

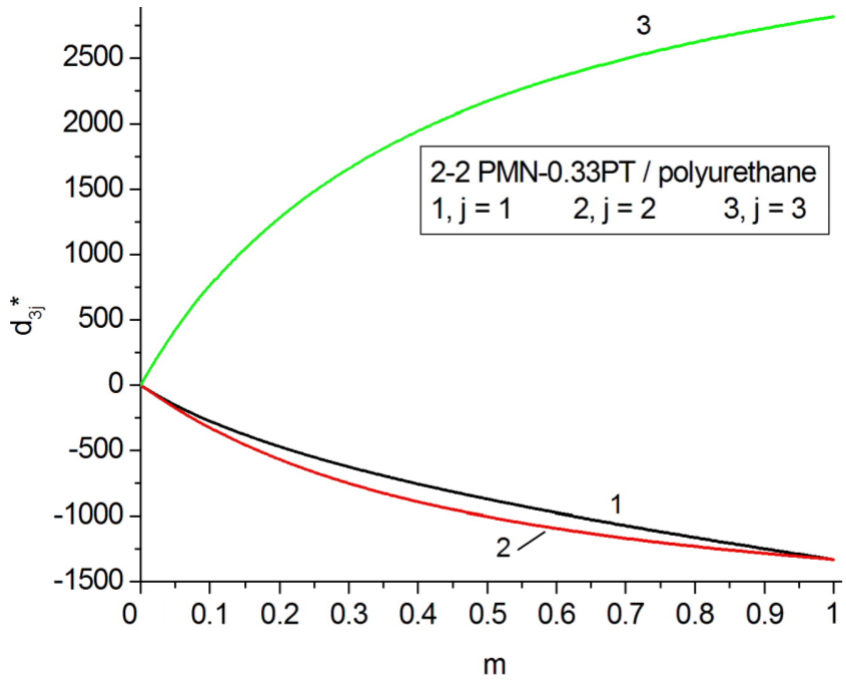

a

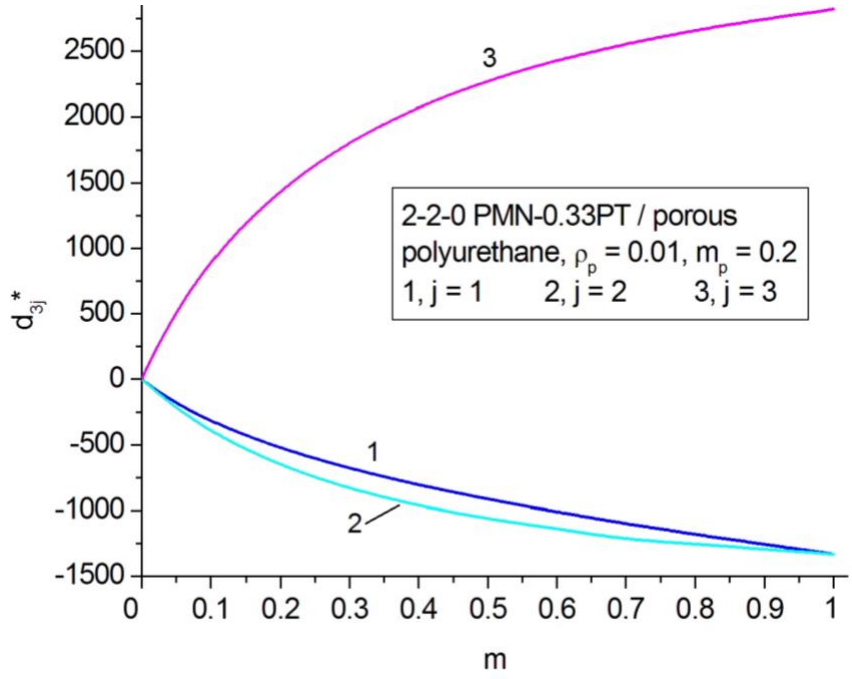

b

Fig. 2 (*continued*)

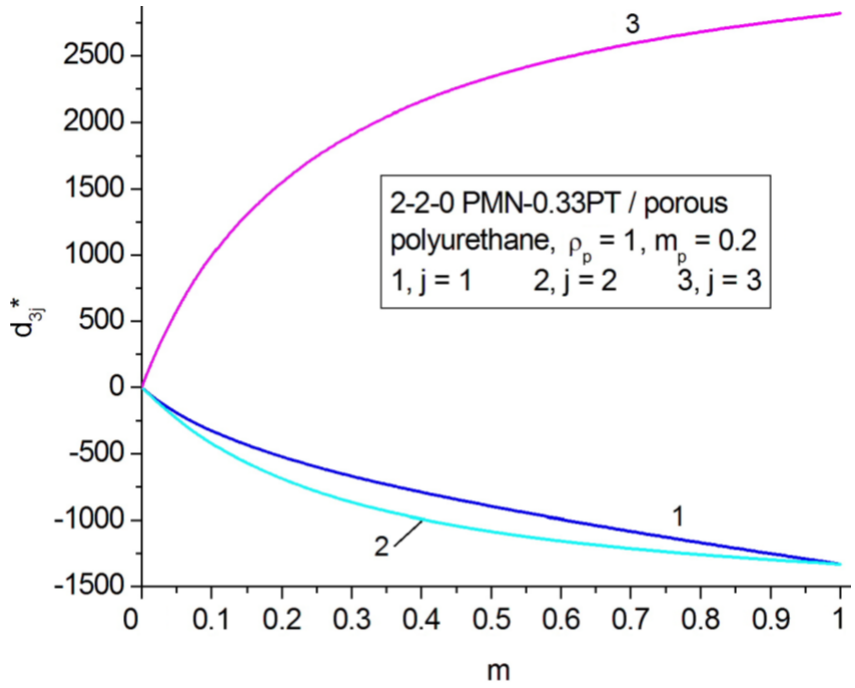
3
2500
2000
1500
1000
500
0
-500
-1000
-1500
d*3j
2-2-0 PMN-0.33PT / porous
polyurethane, ρp = 1, mp = 0.2
1, j = 1 2, j = 2 3, j = 3
1
2
0 0.1 0.2 0.3 0.4 0.5 0.6 0.7 0.8 0.9 1
m

c

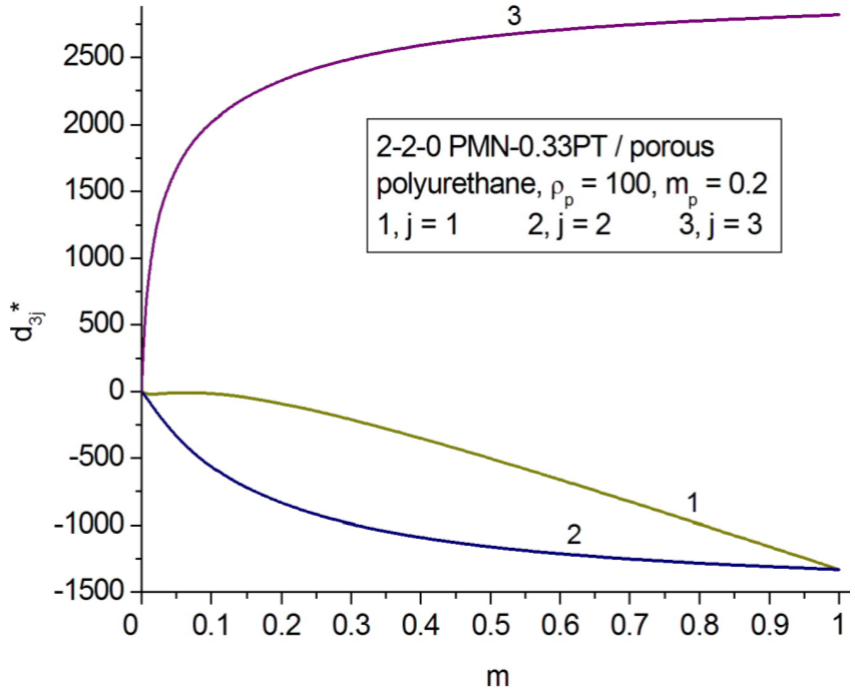
3
2500
2000
1500
1000
500
0
-500
-1000
-1500
d*3j
2-2-0 PMN-0.33PT / porous
polyurethane, ρp = 100, mp = 0.2
1, j = 1 2, j = 2 3, j = 3
1
2
0 0.1 0.2 0.3 0.4 0.5 0.6 0.7 0.8 0.9 1
m

d

Fig. 2

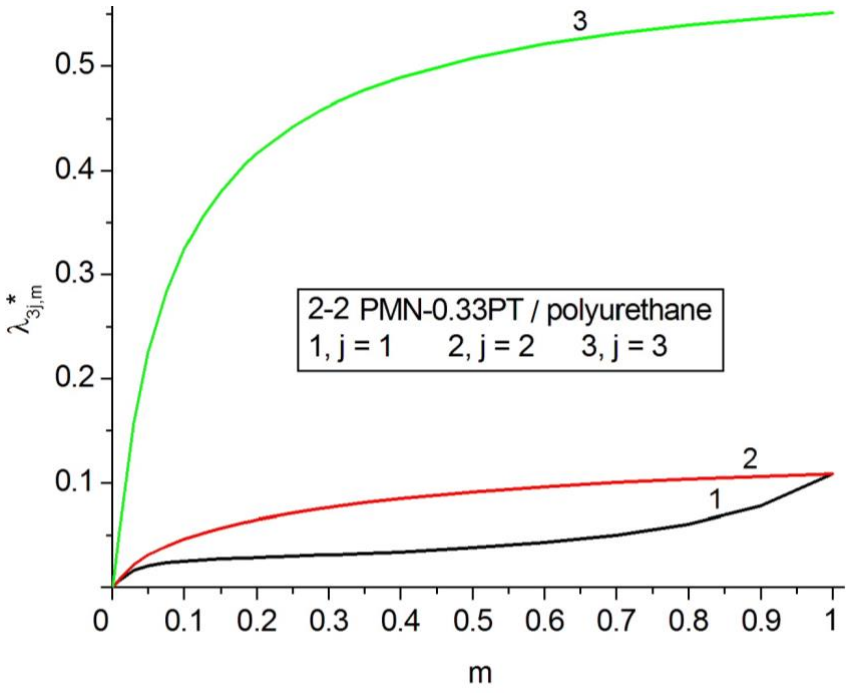

a

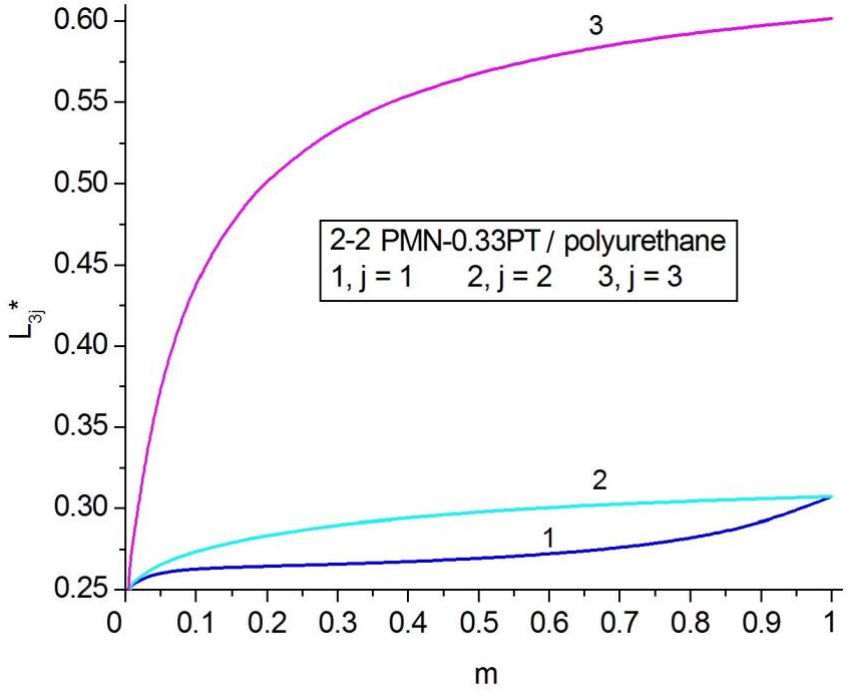

b

Fig. 3 (*continued*)

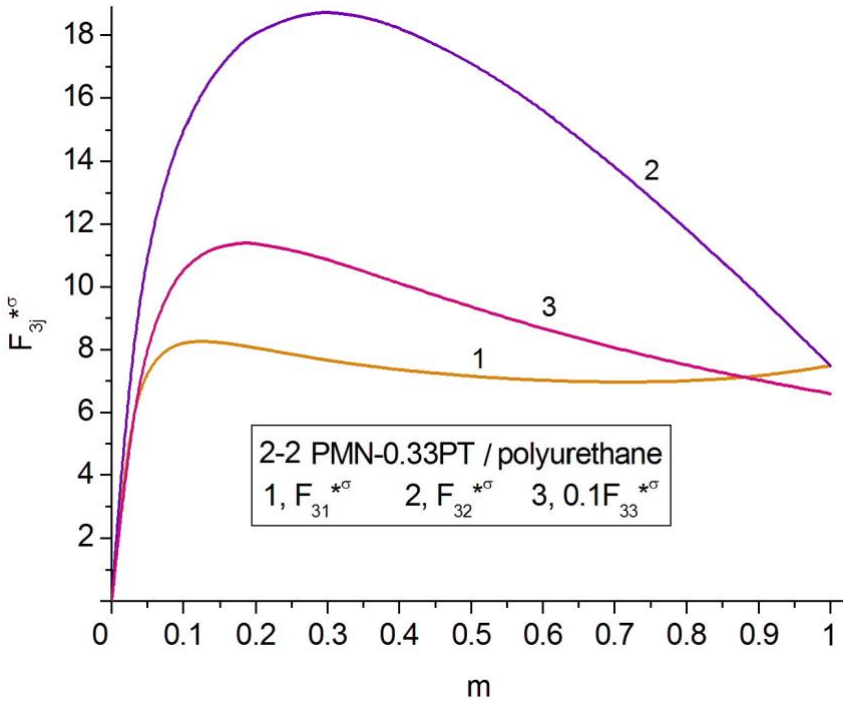

c

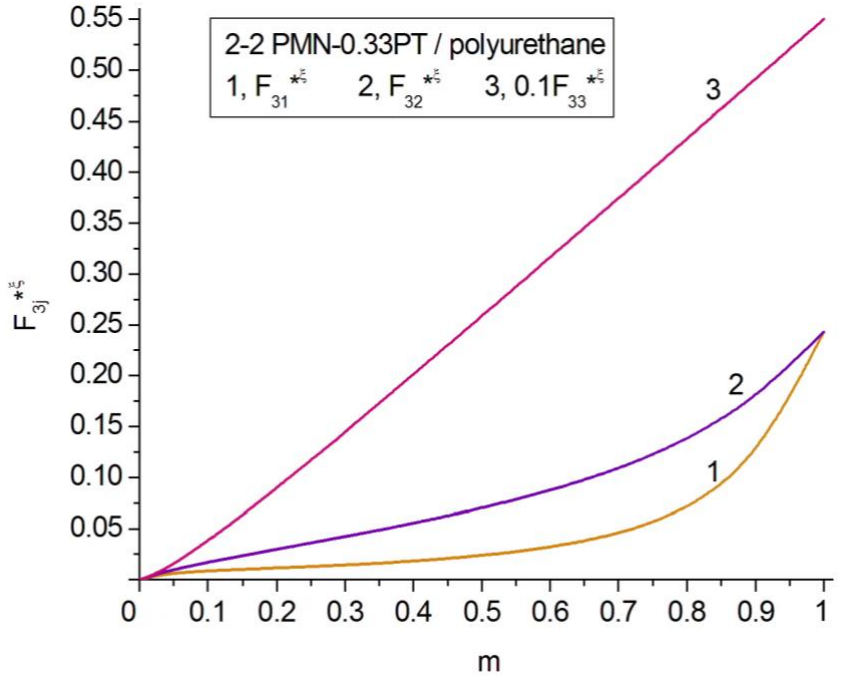

d

Fig. 3 (*continued*)

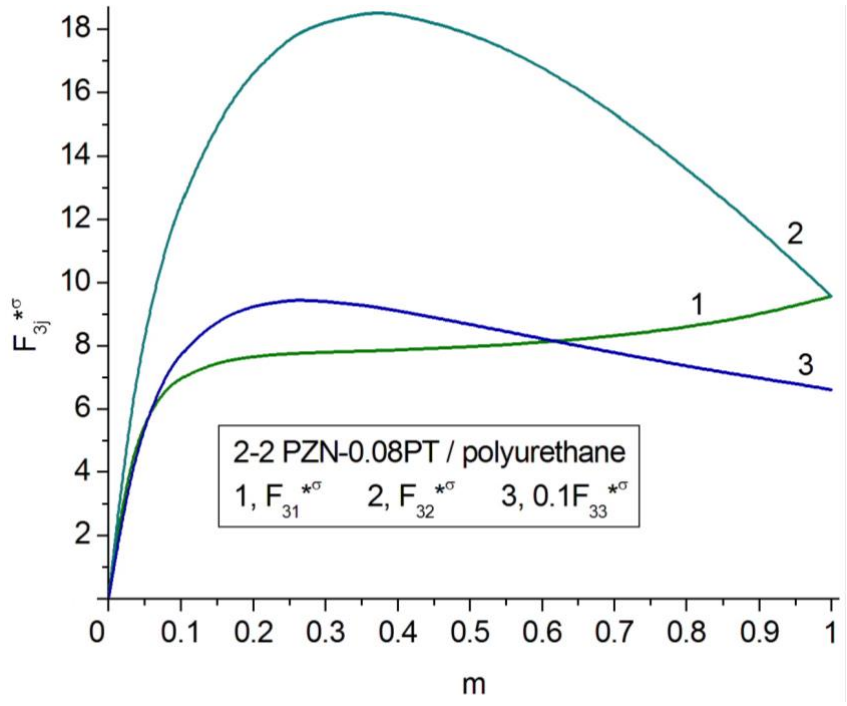
2-2 PZN-0.08PT / polyurethane
1, F31*σ 2, F32*σ 3, 0.1F33*σ
F3j*σ
m

e

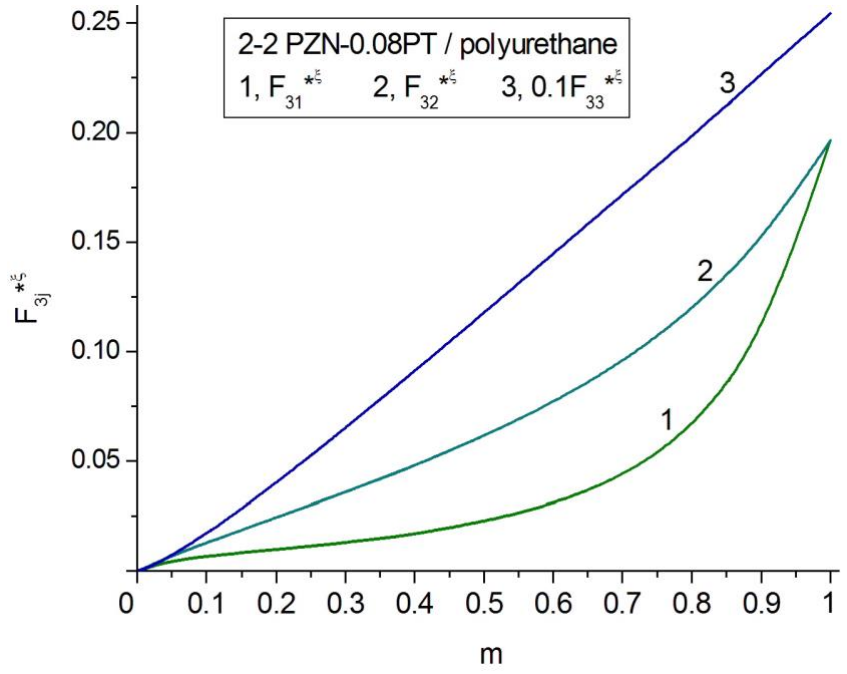
2-2 PZN-0.08PT / polyurethane
1, F31*ξ 2, F32*ξ 3, 0.1F33*ξ
F3j*ξ
m

f

Fig. 3

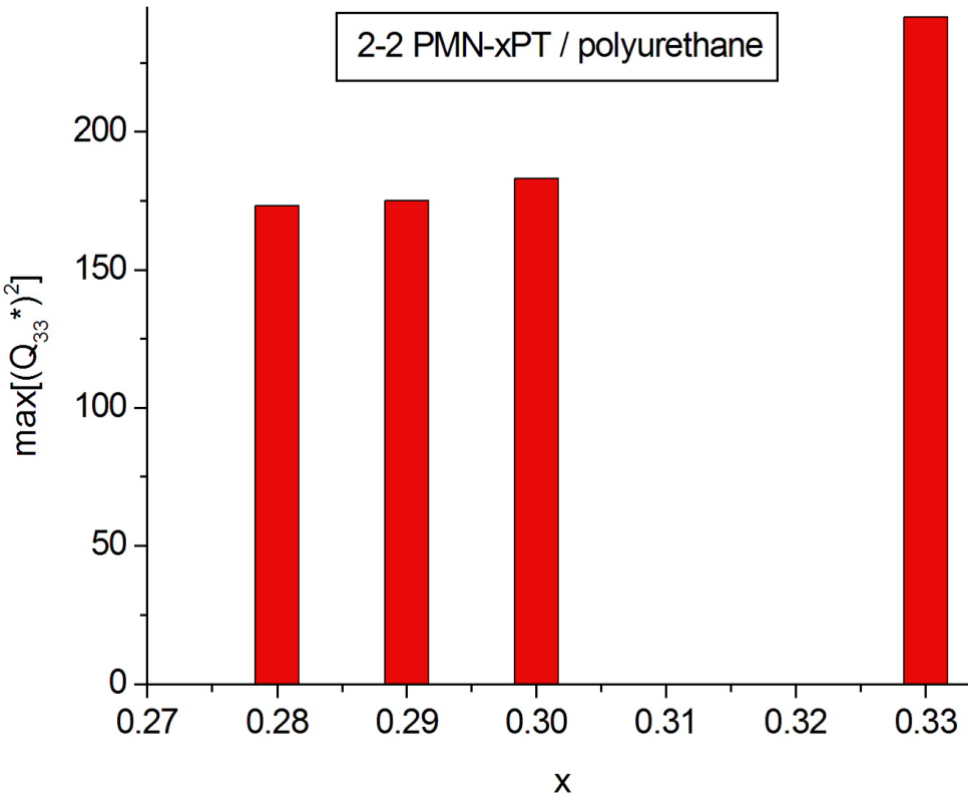
2-2 PMN-xPT / polyurethane
max[(Q33 *)2]
0
50
100
150
200
0.27
0.28
0.29
0.30
0.31
0.32
0.33
x

a

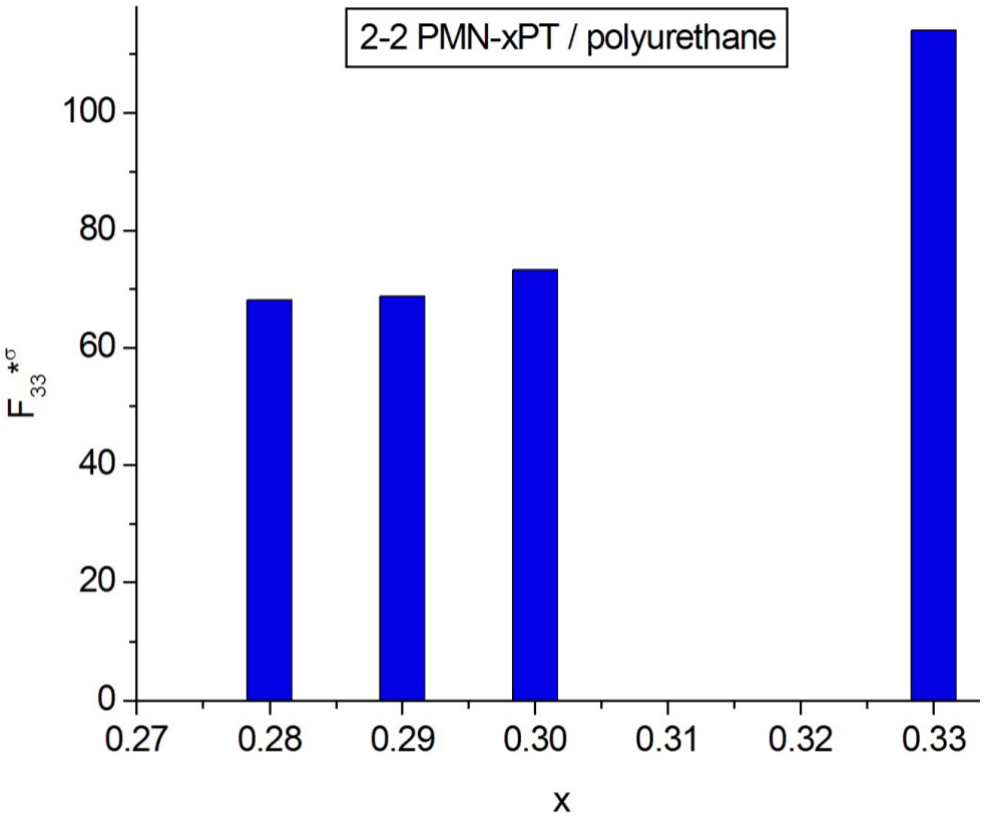
2-2 PMN-xPT / polyurethane
F33 *σ
0
20
40
60
80
100
0.27
0.28
0.29
0.30
0.31
0.32
0.33
x

b

Fig. 4

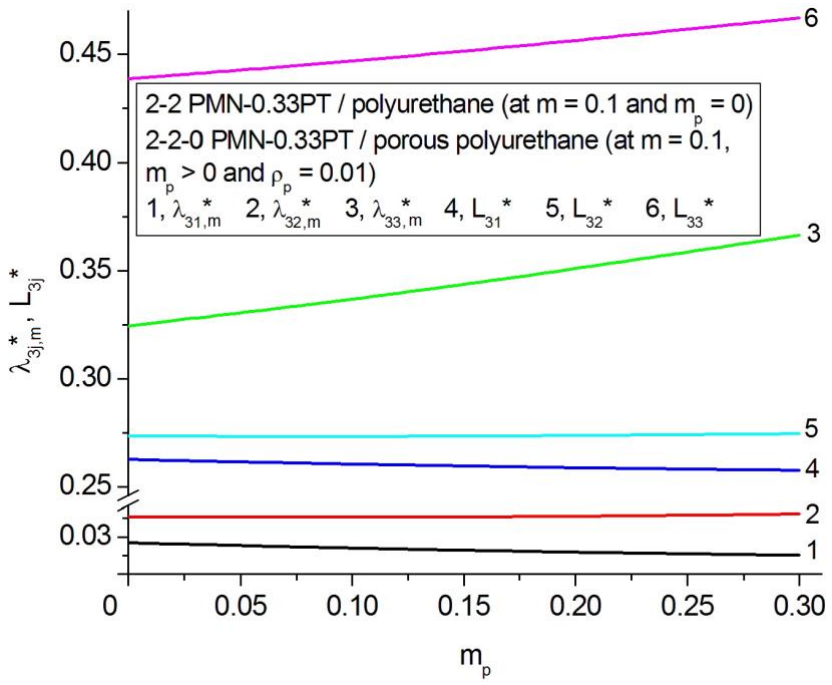

a

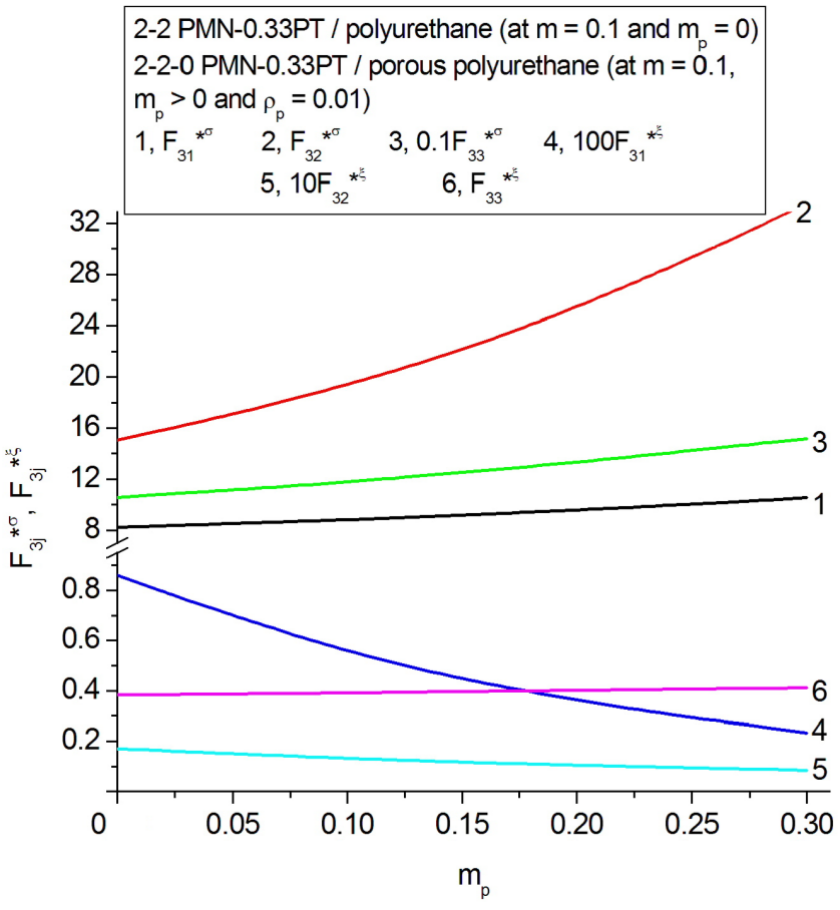

b

Fig. 5 (*continued*)

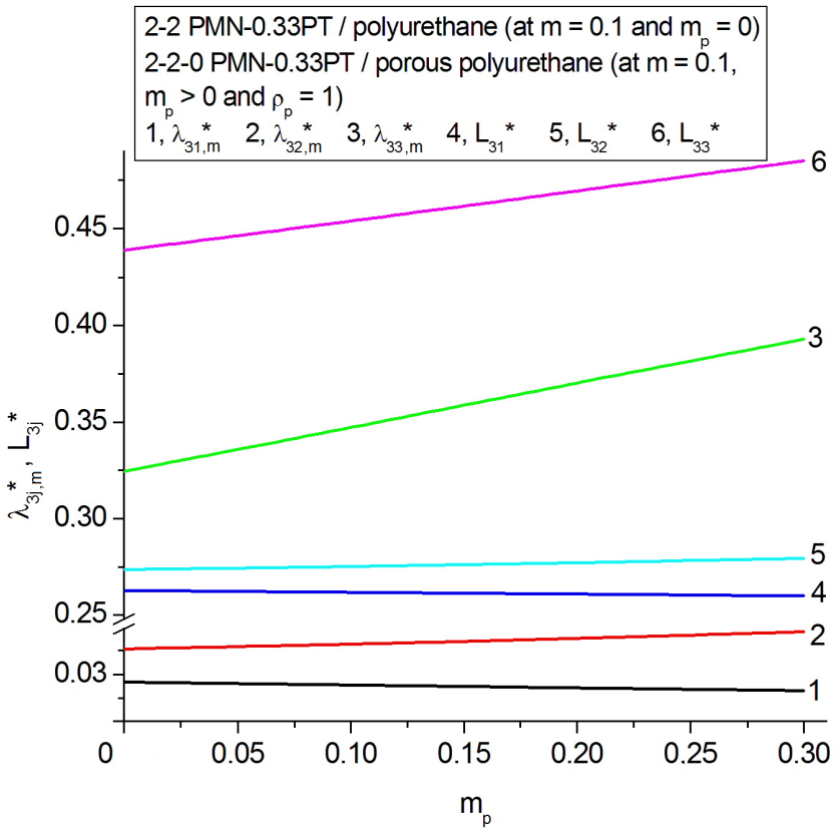

c

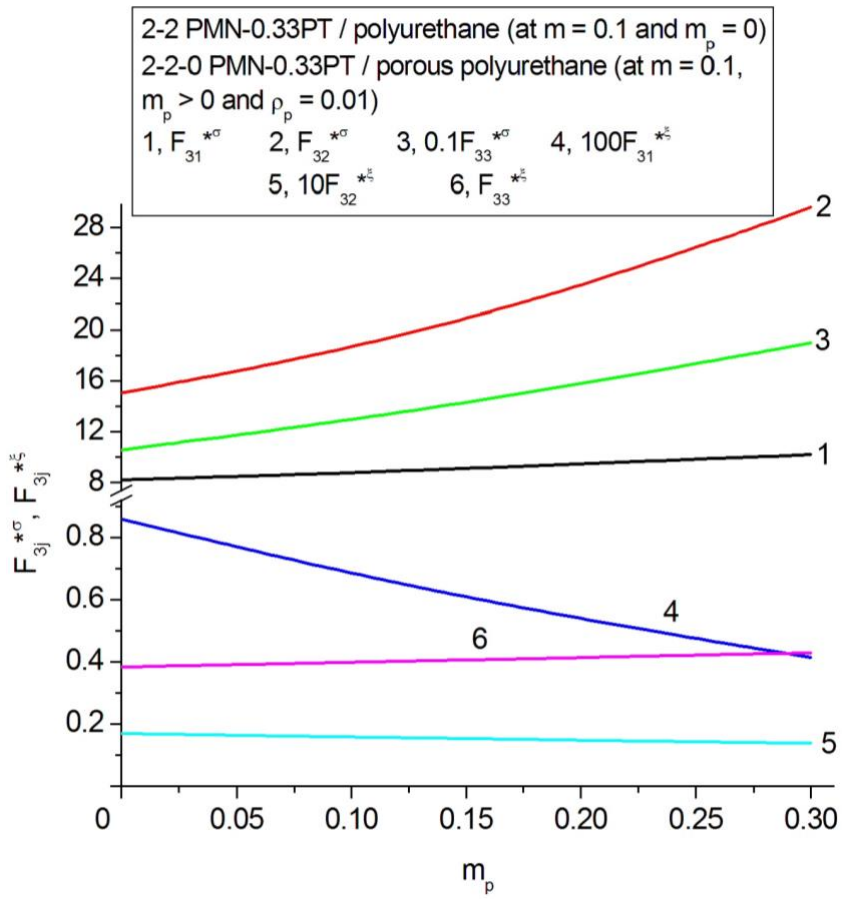

d Fig. 5 (*continued*)

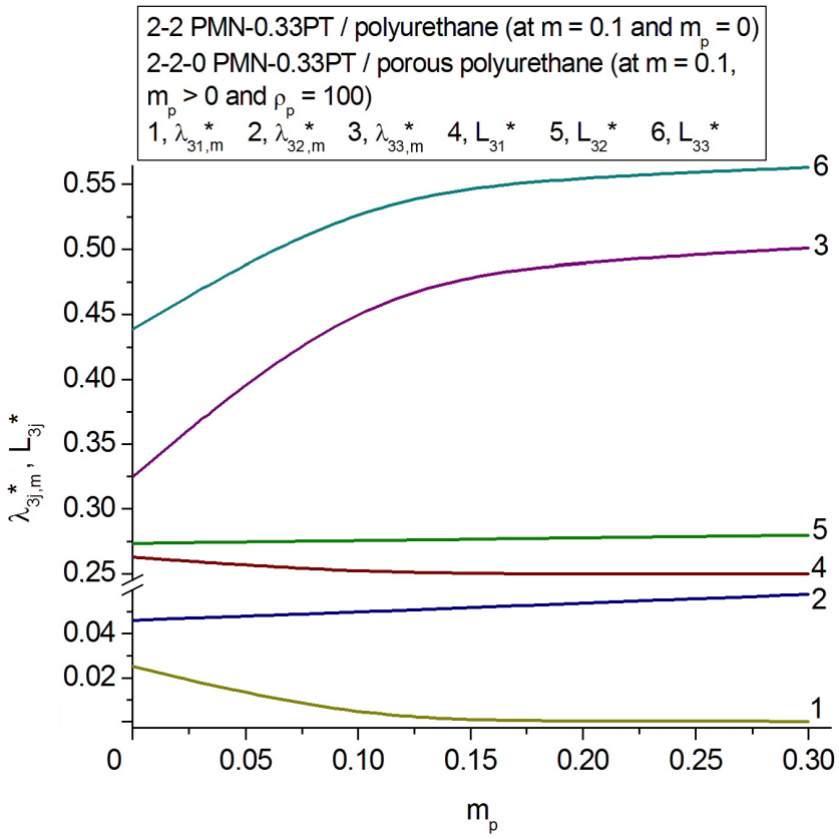

e

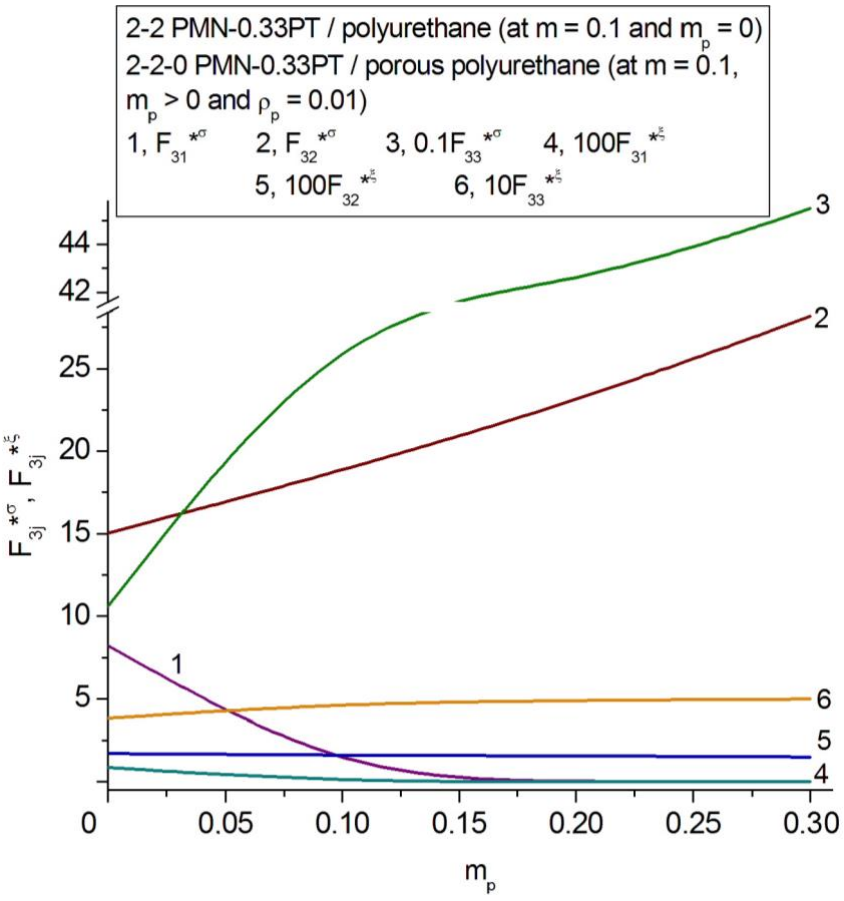

f Fig. 5 (*continued*)

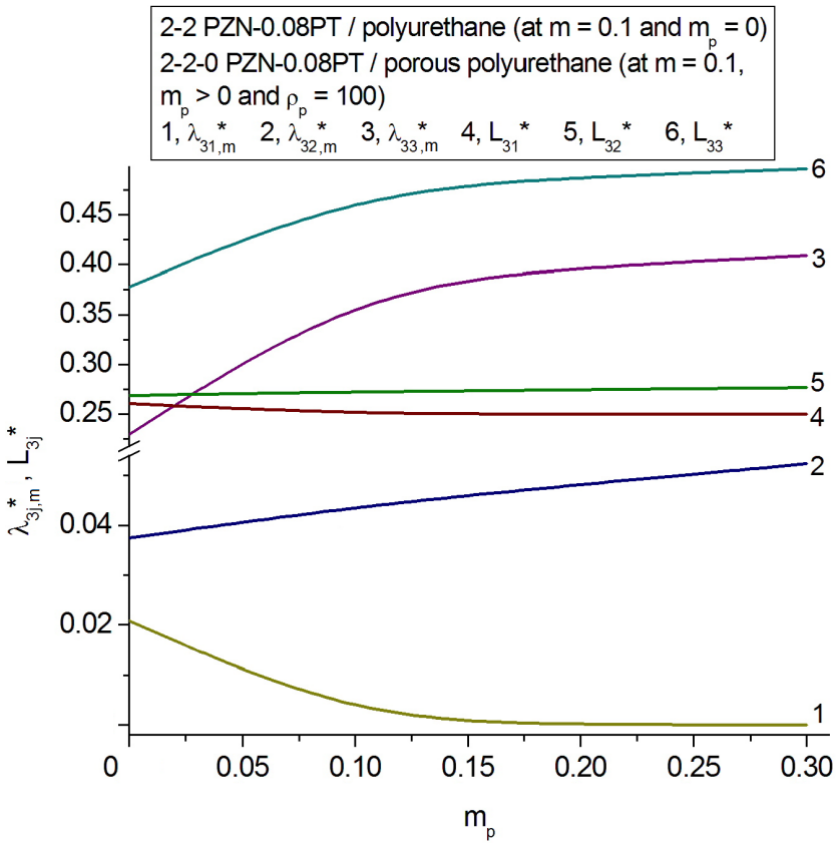
2-2 PZN-0.08PT / polyurethane (at m = 0.1 and m_p = 0)
2-2-0 PZN-0.08PT / porous polyurethane (at m = 0.1, m_p > 0 and ρ_p = 100)
1, λ*_31,m 2, λ*_32,m 3, λ*_33,m 4, L*_31 5, L*_32 6, L*_33
λ*_3j,m , L*_3j
m_p
0.45
0.40
0.35
0.30
0.25
0.04
0.02
0
0.05
0.10
0.15
0.20
0.25
0.30
1
2
3
4
5
6

g

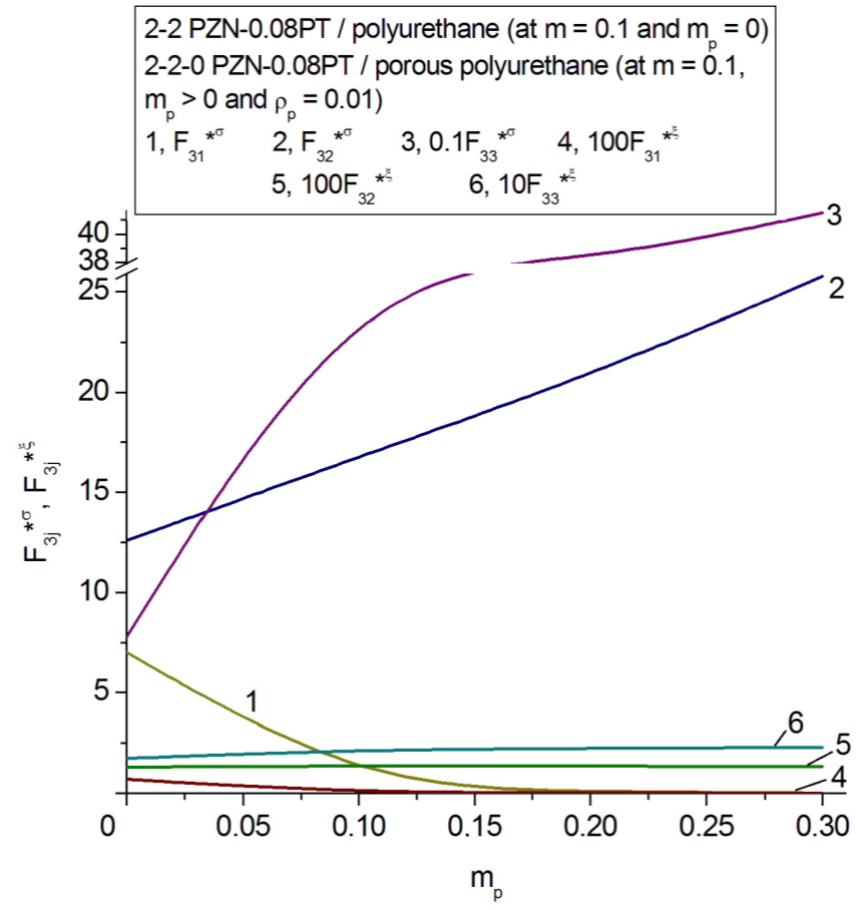
2-2 PZN-0.08PT / polyurethane (at m = 0.1 and m_p = 0)
2-2-0 PZN-0.08PT / porous polyurethane (at m = 0.1, m_p > 0 and ρ_p = 0.01)
1, F*^σ_31 2, F*^σ_32 3, 0.1F*^σ_33 4, 100F*^ξ_31
5, 100F*^ξ_32 6, 10F*^ξ_33
F*^σ_3j , F*^ξ_3j
m_p
40
38
25
20
15
10
5
0
0.05
0.10
0.15
0.20
0.25
0.30
1
2
3
4
5
6

h Fig. 5

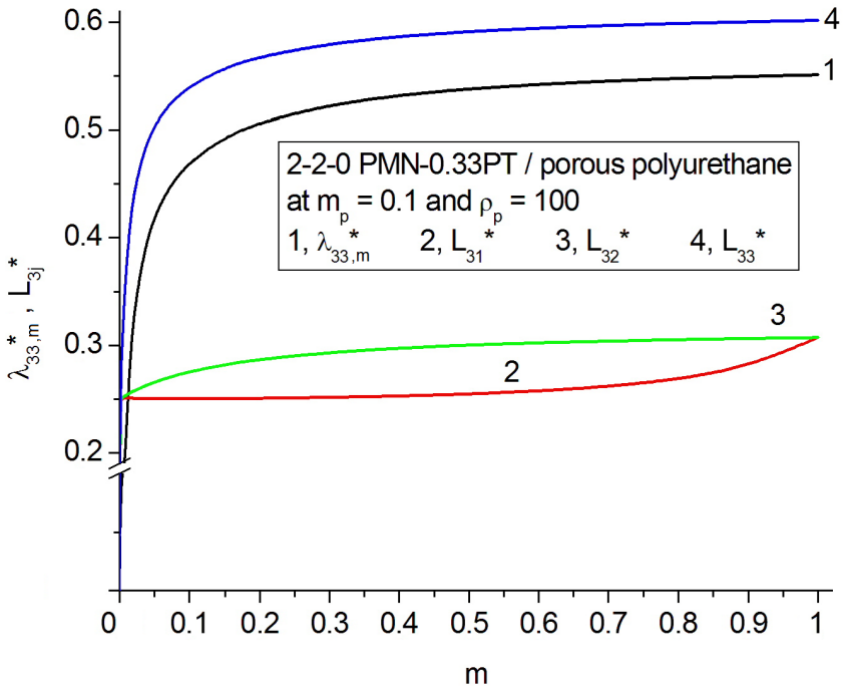

a

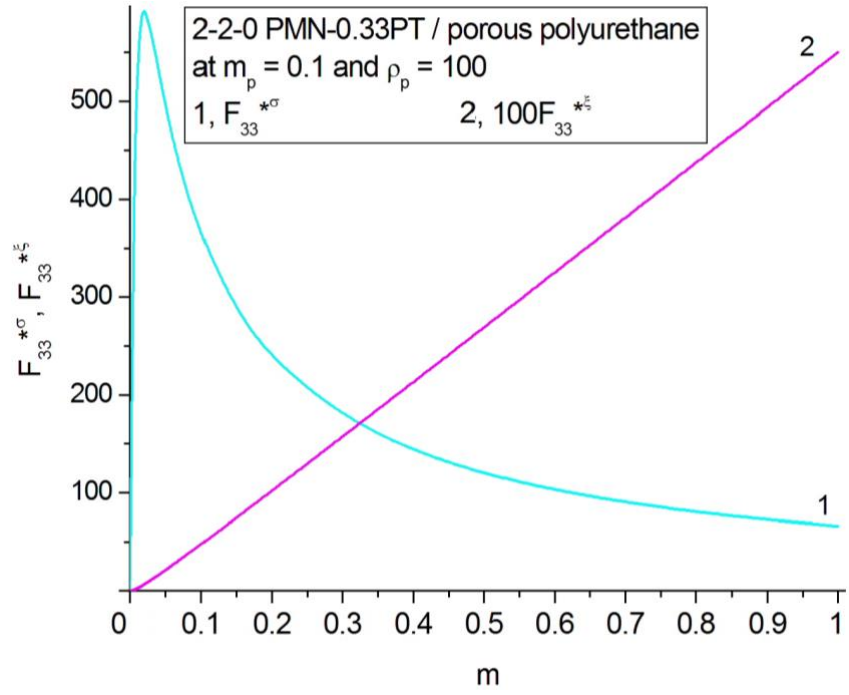

b

Fig. 6 (*continued*)

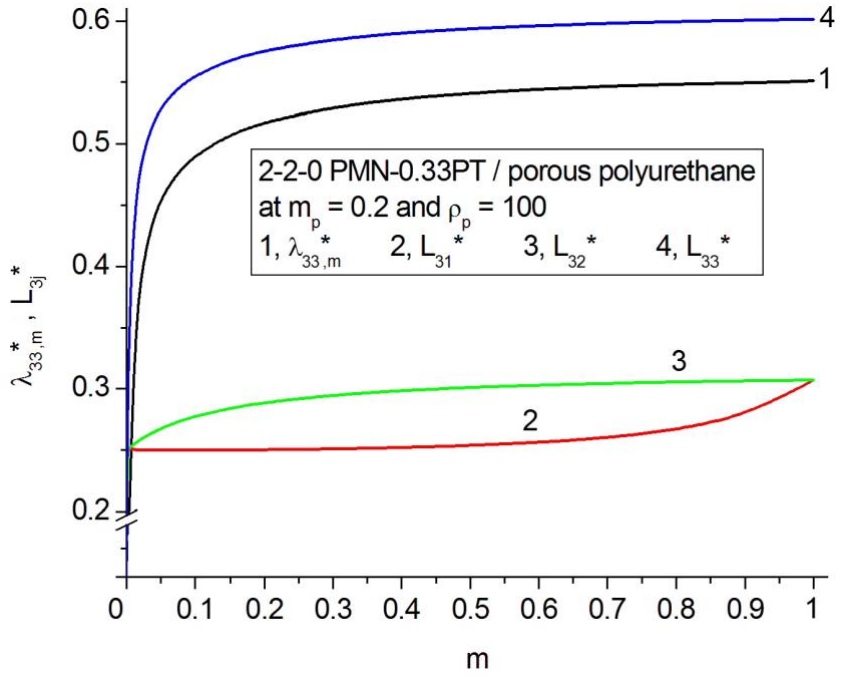

c

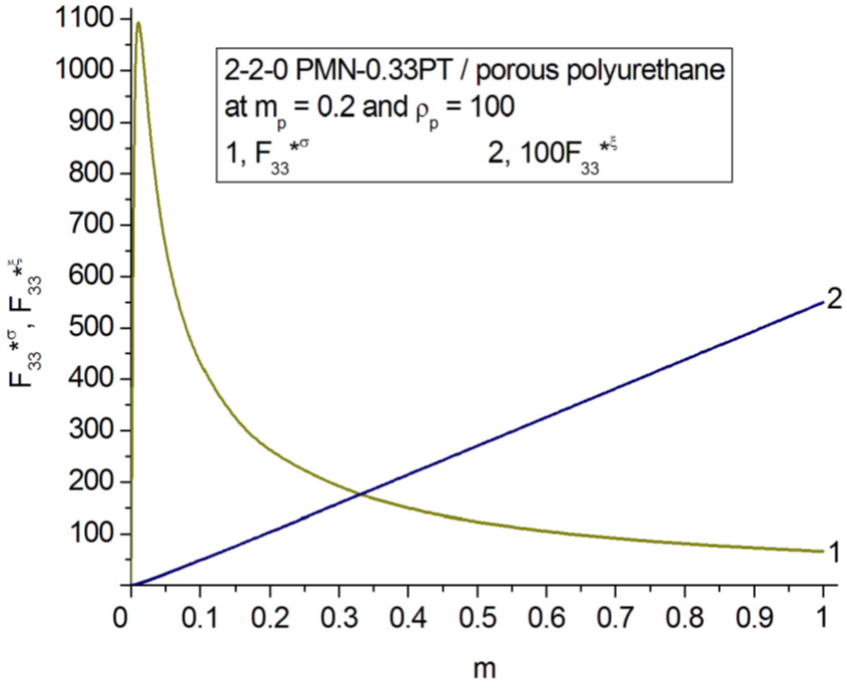

d

Fig. 6 (*continued*)

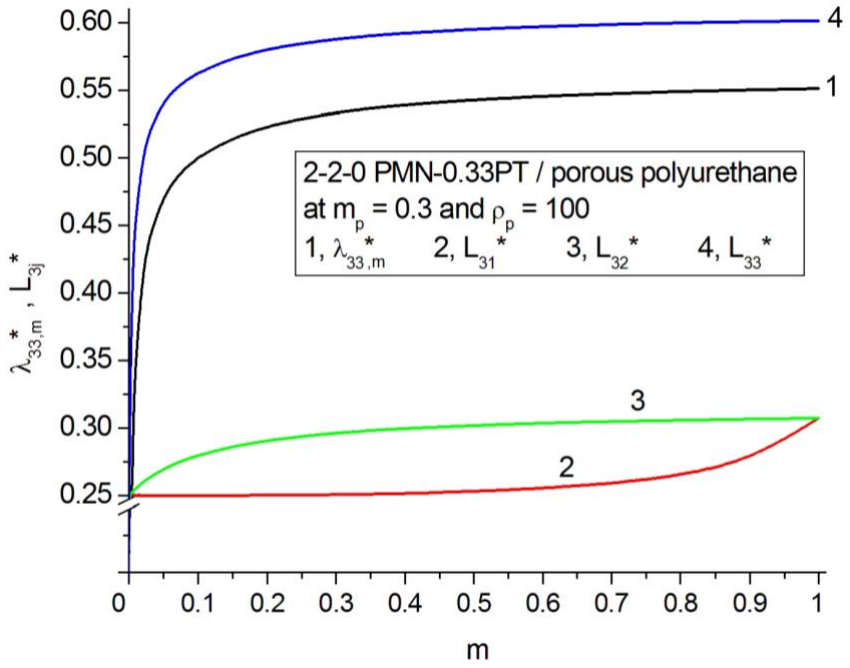
2-2-0 PMN-0.33PT / porous polyurethane
at m_p = 0.3 and ρ_p = 100
1, λ*_33,m 2, L*_31 3, L*_32 4, L*_33
λ*_33,m , L*_3j
m
1
2
3
4

e

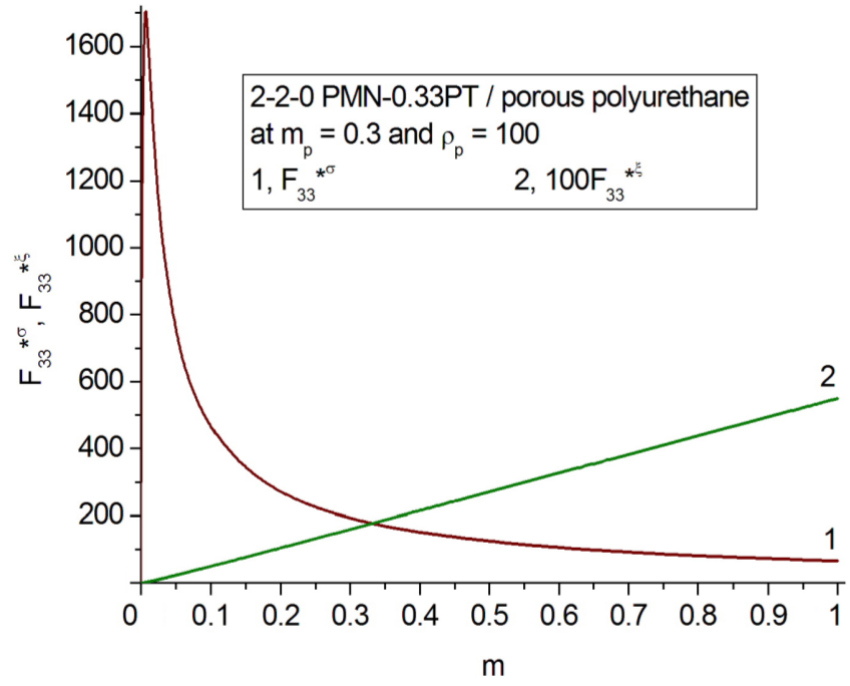
2-2-0 PMN-0.33PT / porous polyurethane
at m_p = 0.3 and ρ_p = 100
1, F*σ_33 2, 100F*ξ_33
F*σ_33 , F*ξ_33
m
1
2

f

Fig. 6

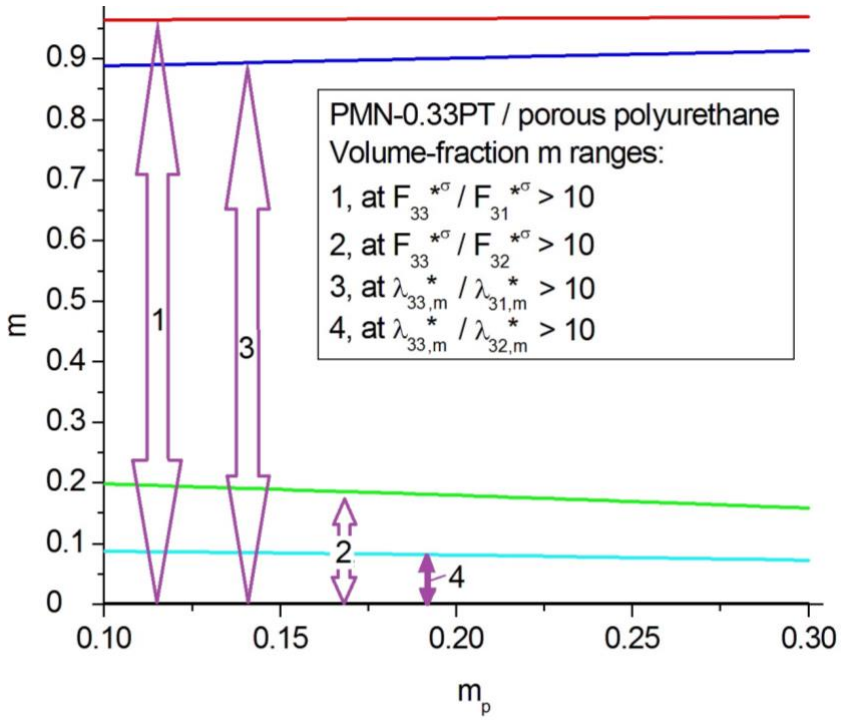
PMN-0.33PT / porous polyurethane
Volume-fraction m ranges:
1, at $F_{33}^{*\sigma} / F_{31}^{*\sigma} > 10$
2, at $F_{33}^{*\sigma} / F_{32}^{*\sigma} > 10$
3, at $\lambda_{33,m}^{*} / \lambda_{31,m}^{*} > 10$
4, at $\lambda_{33,m}^{*} / \lambda_{32,m}^{*} > 10$
m
m_p
1
2
3
4

a

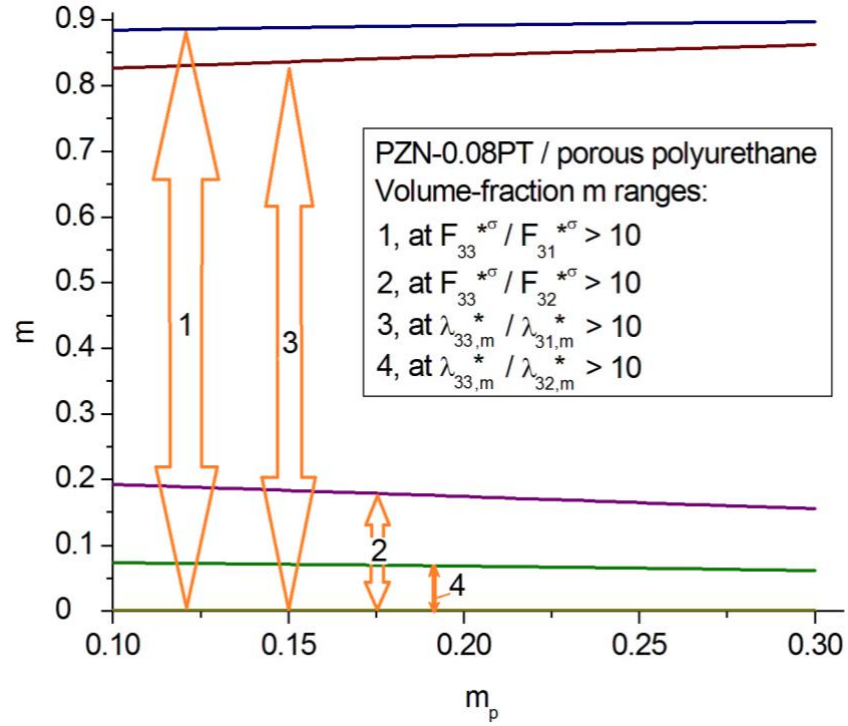
PZN-0.08PT / porous polyurethane
Volume-fraction m ranges:
1, at $F_{33}^{*\sigma} / F_{31}^{*\sigma} > 10$
2, at $F_{33}^{*\sigma} / F_{32}^{*\sigma} > 10$
3, at $\lambda_{33,m}^{*} / \lambda_{31,m}^{*} > 10$
4, at $\lambda_{33,m}^{*} / \lambda_{32,m}^{*} > 10$
m
m_p
1
2
3
4

b

Fig. 7